Nano Research

ISSN 1998-0124 CN 11-5974/O4
https://doi.org/10.26599/NR.2026.94908945

Research Article

Reconstruction mediated lattice oxygen mechanism on hierarchical LDH/MOF nanoarrays for efficient oxygen evolution

Guohao Na[1,§], Mingpeng Chen[1,§](✉), Yuewen Wu[1], Huachuan Sun[1], Dequan Li[1], Tong Zhou[1], Nan Yang[1], Fangyue Chen[1], Yun Chen[1], Yumin Zhang[1], Jin Zhang[1], Di Liu[2](✉), Hui Pan[2], Hao Cui[3], Qingju Liu[1](✉)

[1] Yunnan Key Laboratory for Micro/Nano Materials & Technology, School of Materials and Energy, Yunnan University, Kunming 650091, China

[2] Institute of Applied Physics and Materials Engineering (IAPME), University of Macau, Macao 999078, China

[3] Yunnan Precious Metals Laboratory Co., Ltd., Kunming 650106, China

[§] Guohao Na and Mingpeng Chen contributed equally to this work.

Nano Res., **Just Accepted Manuscript** • https://doi.org/10.26599/NR.2026.94908945

https://www.sciopen.com/journal/1998-0124 on Jun. 17, 2026

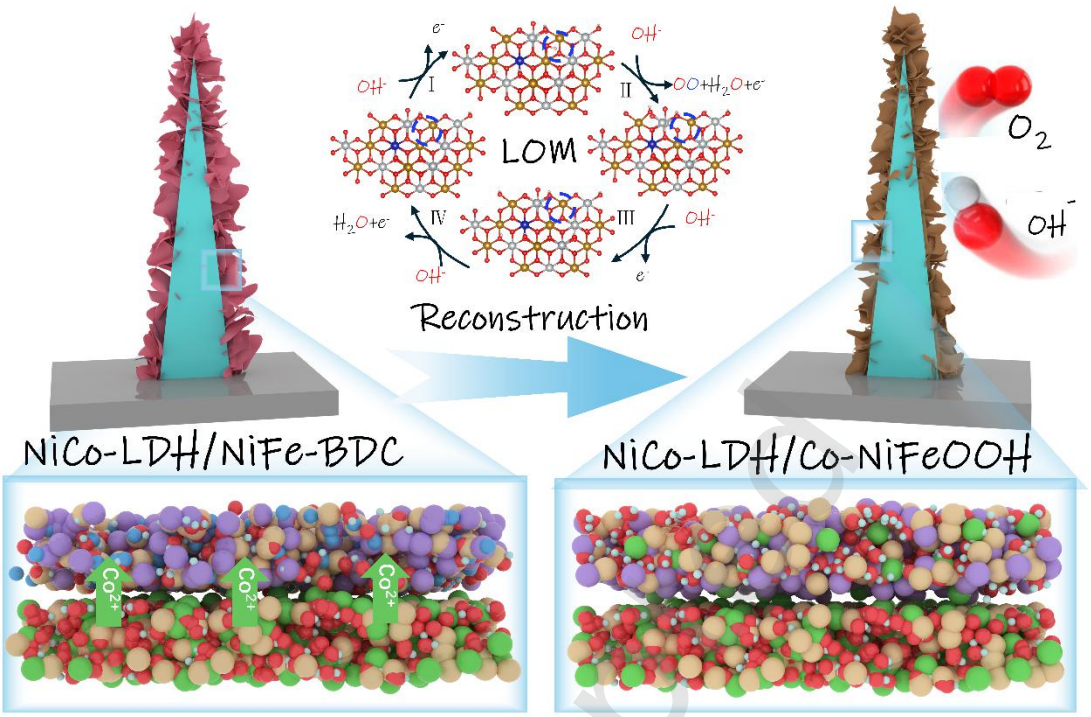

Co diffusion–induced reconstruction of NiCo-LDH/NiFe-BDC forms Co-NiFeOOH active phases, activating the lattice oxygen mechanism for enhanced OER performance.

Research Article

Reconstruction mediated lattice oxygen mechanism on hierarchical LDH/MOF nanoarrays for efficient oxygen evolution

Guohao Na[1,§], *Mingpeng Chen*[1,§,*], *Yuewen Wu*[1], *Huachuan Sun*[1], *Dequan Li*[1], *Tong Zhou*[1], *Nan Yang*[1], *Fangyue Chen*[1], *Yun Chen*[1], *Yumin Zhang*[1], *Jin Zhang*[1], *Di Liu*[2,*],, *Hui Pan*[2], *Hao Cui*[3], and *Qingju Liu*[1,*]

[1] Yunnan Key Laboratory for Micro/Nano Materials & Technology, School of Materials and Energy, Yunnan University, Kunming 650091, China

[2] Institute of Applied Physics and Materials Engineering (IAPME), University of Macau, Macao 999078, China

[3] Yunnan Precious Metals Laboratory Co., Ltd., Kunming 650106, China

[§] Guohao Na and Mingpeng Chen contributed equally to this work.

Received: 22 January 2026; **Revised:** 13 March 2026; **Accepted:** 17 June 2026

Address correspondence to Mingpeng Chen, mpchen@ynu.edu.cn; Di Liu, diliu@um.edu.mo; Qingju Liu, qjliu@ynu.edu.cn

Cite this article: *Nano Research*, 2026, 19, 94908945 https://doi.org/10.26599/NR.2026.94908945

Abstract:

Developing highly active, cost-effective, and durable nonprecious electrocatalysts is critical for advancing alkaline water electrolysis. However, the origin of activity and reaction pathway are significantly influenced by anode reconstruction effects, which remain unclear and expedite the further exploration. Herein, we propose a hierarchical catalyst, composed of bimetallic metal-organic framework (MOF) nanosheets supported on layered double hydroxide (LDH) nanorods. During the oxygen evolution reaction (OER), Co ions diffuse to the surface and accelerates the structural evolution, simultaneously inducing the transformation of NiFeOOH from γ-phase to β-phase and lowering the reconstruction voltage from 1.5 V to 1.3 V. The resultant catalyst Nickel–cobalt layered double hydroxide supported on NiFe–BDC (BDC = 1,4-benzenedicarboxylate) metal–organic framework (NiCo-LDH/NiFe-BDC). achieves ultralow overpotentials of 180 and 255 mV at 10 and 500 mA/cm^2, respectively, and maintains stable operation at 500 mA/cm^2 over 500 h. The pH-dependent OER performance, molecular probe analysis, online measurement of ^{18}O-labelled catalyst, and theoretical calculations collectively indicate that the generated Co-NiFeOOH serves as the active species and the reduced Ni–O–Fe bonding activates lattice oxygen mechanism (LOM). This work not only offers an insightful view on OER-driven reconstruction process, but also correlates it to the catalyst's electronic structure and the reaction mechanism, which may inspire innovative design of OER catalysts.

Keywords: oxygen evolution reaction, reconstruction, lattice oxygen mechanism, metal–organic framework.

Introduction

Alkaline water electrolysis is an emerging energy conversion technology for large-scale green hydrogen production However, its efficiency faces critical

bottlenecks due to the sluggish kinetics of oxygen evolution reaction (OER), which involves four-electron transfer steps.[1-4] Thus, efficient and precious-metal-free catalysts which accelerate the OER kinetics are highly anticipated to replace the commercial RuO_2 or IrO_2 for widespread applications.[5] Nowadays, numerous 3d transition-metal (Fe, Co, and Ni) materials, such as metal oxides,[6] metal (oxy)hydroxides,[7] metal sulfides,[8] and metal-organic frameworks (MOFs)[9] have emerged as promising alkaline OER catalysts. Nevertheless, most reported systems exhibit overpotentials exceeding 200 mV at 10 mA cm^{-2} and 300 mV at 500 mA cm^{-2}. Optimizing the reaction process is an effective way to regulate the catalytic performance, which needs deeper understandings on the reaction mechanisms[10-12]

In general, two possible reaction mechanisms are involved in OER, including the adsorbate evolution mechanism (AEM) and lattice oxygen mechanism (LOM).[13] AEM prevails when metal sites serve as redox centers and OER proceeds via multiple adsorbed intermediates, such as *OH, *O, *OOH.[14] The adsorption energies of these intermediates exhibit a linear scaling relationship, impeding the improvement of OER performance. In contrast, LOM utilizes lattice oxygen sites as redox centers, which empower the catalyst bypassing the scaling relation through the direct O–O coupling.[15] Therefore, the activation of lattice oxygen can fundamentally present higher OER performance.[16] State-of-the-art NiFe-based materials have been already recognized as the most effective OER electrocatalysts in alkaline condition due to their excellent activity and stability.[17-19] However, their reaction mechanisms remain a hot debating topic. Rational design of NiFe-based materials to trigger the LOM pathway can not only offer ideal models for unraveling the structure-activity relationship, but also deliver outstanding OER performance for industrial applications.[20]

Nowadays, researchers have reached a broad consensus that metal oxyhydroxides, derived from structural evolution during alkaline OER process, work as the real active species.[21, 22] For example, Qiu et al. demonstrated that a

Ni_2P/Fe_2P heterostructure with rich phosphorus vacancies undergoes deep reconstruction to NiOOH/FeOOH, activating lattice oxygen participation and enhancing activity.[23] Nevertheless, elucidating the evolution of active sites and intermediates on NiFe-based catalysts is essential for identifying pathway.[24-26] Qian et al. proposed that phosphorus doping in the NiFeP catalyst facilitates the formation of active β-Ni(Fe)OOH phase, promoting the *OH deprotonation and the O−O coupling to generate *OO intermediates.[27] Despite these advances, precisely regulating surface properties via structural design of the pre-catalysts remains challenging.

Herein, we innovatively design a hierarchical NiCo-LDH/NiFe-BDC architecture, where uniform NiFe-MOF nanosheets are supported on NiCo-LDH nanorods. Upon anodic potential, rapid Co ions' diffusion to the surface accelerates the surface reconstruction, lowering the reconstruction voltage. In situ Raman study reveals that the adaptive Co-doping induces the phase transformation of NiFeOOH from γ-phase to β-phase. Consequently, NiCo-LDH/NiFe-MOF demonstrates exceptionally low overpotentials of 180 and 255 mV at current densities of 10 and 500 mA/cm², respectively, and exhibits excellent stability over 500 h at an industrial current density, surpassing the commercial RuO_2. The combination of pH-dependent performance, molecular probe analysis, ^{18}O-isotopic labelling mass spectroscopy, and theoretical calculations prove that the lattice oxygen activated by the weakened Ni−O−Fe participates in the reaction process, illustrate the LOM mechanism. Our results highlight the role of hierarchical MOF/LDH nanoarrays and structural evolution in modulating the OER pathway, providing guidance on the rational design of OER electrocatalysts from design.

Results and Discussion

As illustrated in **Fig. 1a**, the hierarchical NiCo-LDH/NiFe-BDC nanoarrays were successfully synthesized through a simple two-step hydro-/solvo-thermal reaction.

Initially, NiCo-LDH nanorods were uniformly grown on a nickel foam (NF) substrate. Subsequently, Ni^{2+}, Fe^{3+}, and benzene-1,4-dicarboxylic acid (1,4-BDC) were introduced to prepare the polymetallic NiFe-BDC nanosheets over the NiCo-LDH surface. Upon subsequent cyclic voltammetry (CV) activation, NiCo-LDH/NiFe-BDC undergoes a surface reconstruction process, while Co atoms migrate toward the surface, leading to the formation of active Co-incorporated NiFeOOH (Co-NiFeOOH) species. Notably, the color of the electrode darkens significantly after the surface reconstruction (Fig. S1).

Scanning electron microscopy (SEM) images reveal that NiCo-LDH exhibits a needle-like nanorod morphology, and some nanorods assemble into spherical structures with a diameter of approximately 10 μm (Fig. S2). Transmission electron microscopy (TEM) images show that these nanorod have an average diameter of ~100 nm (Fig. S3a, b). High-resolution TEM (HRTEM) images display clear lattice fringes with a spacing of 0.24 nm, which can be attributed to the (111) crystal plane of NiCo-LDH (Fig. S3c, d). As shown in **Fig. 1b**, the NiFe-BDC nanosheets are more uniform and smaller, densely coated on the nanorods. The thickness of the outer layer NiFe-BDC is around 80 nm, and a distinct heterointerface between NiCo-LDH and NiFe-BDC can be clearly identified (**Fig. 1c, d**). The characteristic lattice with a spacing of 0.41 nm observed in the HRTEM image can be indexed to the (40-1) crystal plane of NiFe-BDC, while NiCo-LDH retains its original morphology and crystalline structure (Fig. S4).

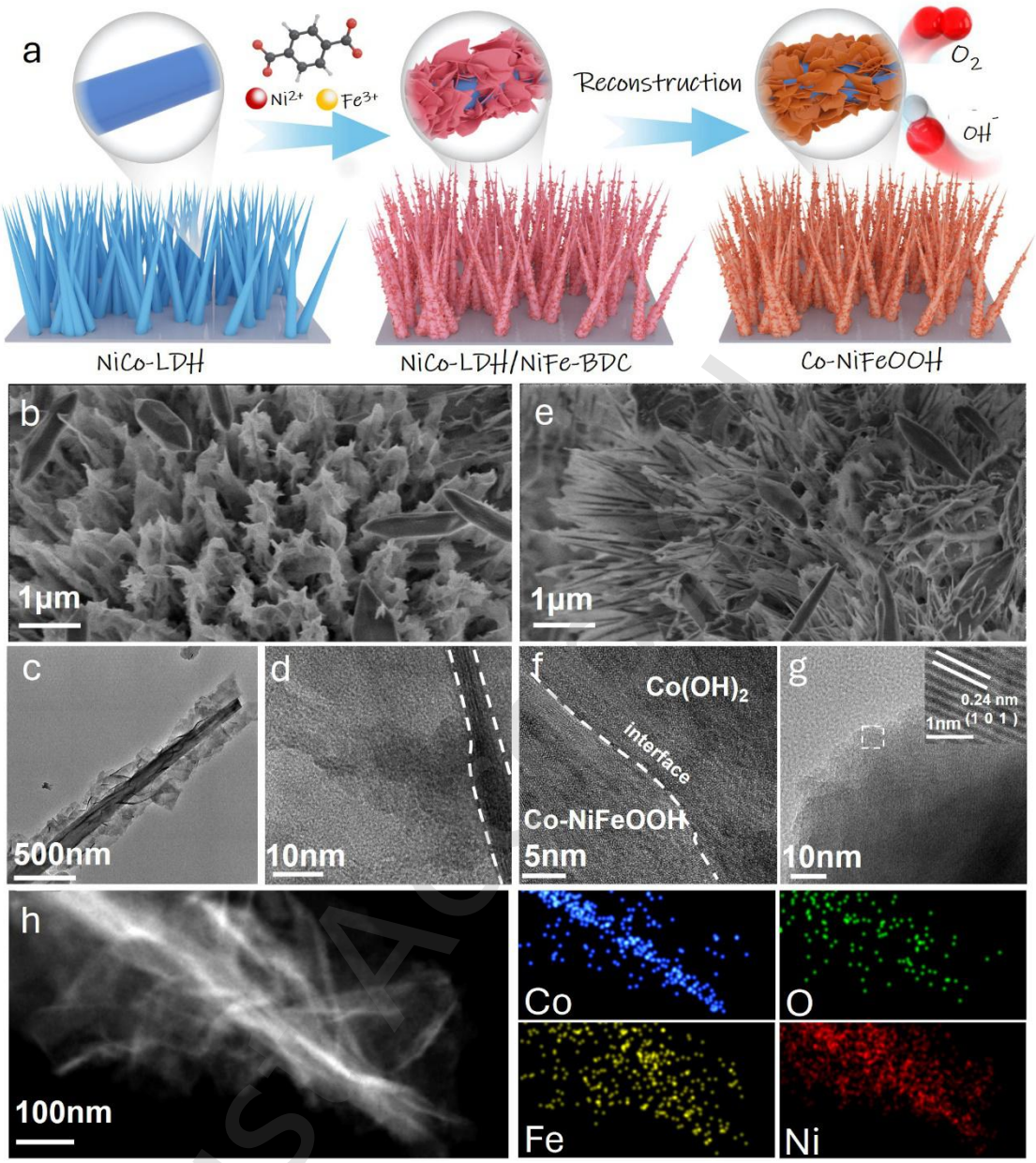

Fig. 1 Preparation and structural characterization. (a) Schematic illustration of the synthetic route and reconstruction for NiCo-LDH/NiFe-BDC. (b) SEM, (c) TEM and (d) HRTEM images of NiCo-LDH/NiFe-BDC. (e) SEM, (f, g) HRTEM images and (h) EDS elemental mapping of reconstructed NiCo-LDH/NiFe-BDC.

It is known that structural evolution commonly occurs during the OER process. SEM image reveals a cross-linked network composed of hierarchical nanorods with consistent widths, and the increased surface roughness indicates surface reconstruction, which is beneficial for the exposure of active sites and the

electrolyte/bubble diffusion (**Fig. 1e**). In addition, a distinct interfacial boundary is observed in the HRTEM image, showing the crystalline structure of NiCo-LDH remains unchanged, while distinct lattices with spacings of 0.24 nm and 0.21 nm emerge near the surface and interface, respectively, corresponding to the (101) and (111) planes of orthorhombic NiFeOOH. This result confirms the successful structural conversion from NiCo-LDH/NiFe-BDC to NiCo-LDH/Co-NiFeOOH (**Fig. 1g** and S5). The N_2 adsorption–desorption isotherms were recorded to evaluate the pore structure and specific surface area of as-prepared samples. As shown in Figure S6, the isotherms can be classified as type II curves with an H3-type hysteresis loop, indicating the presence of mesoporous structures in all catalysts. The abundant mesopores and micropores endow the catalysts with relatively high specific surface areas of 62, 104, and 89 $m^2 g^{-1}$, respectively (Table S1).

To further study the structure and composition of pristine and post-OER samples, X-ray diffraction (XRD) and energy dispersive X-ray spectroscopy (EDS) were employed. As shown in Fig. S7a, the XRD pattern of NiCo-LDH exhibits main diffraction peaks which can be well indexed to the $Co(OH)_2$ structure (JCPDS No. 50-0827). Meanwhile, the XRD pattern of NiCo-LDH/NiFe-BDC shows additional peaks at 8.9° and 18.1°, agreeing well with the (110) and (220) planes of the reported MOF structure (CCDC No. 985792), consistent with the HRTEM observations (Fig. S7b). The lattice constants obtained from the refinement of NiFe-BDC are consistent with the indexed spectra (Fig. S7c). Furthermore, the elemental mappings in Fig. S8 confirm the uniform distribution of Co, Ni and O elements in a single NiCo-LDH nanorod, while Ni, Fe, and O elements are homogenously distributed in the outer shell of NiCo-LDH/NiFe-BDC (Fig. S9). After the alkaline OER process, outward Co diffusion is evident, while other elements in NiCo-LDH/NiFe-BDC remains their distribution, which is effectively supported by line-scan EDS analysis (Fig. S10).

Then, X-ray photoelectron spectroscopy (XPS) was employed to probe the near-surface electronic states of NiCo-LDH/NiFe-BDC pre- and post- activation. The

XPS survey spectra confirm the presence of Ni, Fe, Co, and O elements (Fig. S11). These elements in pre-catalysts present similar electronic states, suggesting the successful preparation of LDH/MOF hybrid (Fig. S12). The high-resolution Fe 2p XPS spectra of the initial NiCo-LDH/NiFe-BDC can be deconvoluted into three sets of peaks, including Fe^{2+} (710.0/722.6 eV), Fe^{3+} (713.3/726.1 eV), and satellite peaks (717.1/730.8 eV). Ni 2p XPS spectra show peaks attributed to Ni^{2+} (855.6/873.2 eV), Ni^{3+} (857.0/875.7 eV), and satellite peaks (861.9/880.0 eV) as well.[28] Noteworthily, the binding energy of Fe $2p_{3/2}$ shifts to a higher value by 0.8 eV, and the similar phenomenon is observed in the Ni XPS spectrum with a positive shift of 0.9 eV (**Fig. 2a, b**), implying the formation of high-valence metals sites, which may accelerate the OER kinetics.[29] For pristine NiCo-LDH and NiCo-LDH/NiFe-BDC, the Co 2p spectra show three sets of peaks, corresponding to Co^{3+} (780.9/796.7 eV), Co^{2+} (783.3/799.2 eV), and satellite peaks (787.1/803.1 eV). After the OER process, the Co^{2+} peaks disappeared, proving that Co element is completely oxidized into high-valence Co^{3+} (**Fig. 2c**), indicating its incorporation into the active species. Additionally, the O 1s spectra of pristine samples show two peaks at 531.6 and 532.7 eV, corresponding to M-OH and adsorbed O species (O_{abs}) **(Fig. S11d)**. After OER, a new peak corresponding to lattice oxygen (O_L) appears at 529.8 eV, which is crucial for modulating the LOM mechanism.[30, 31]

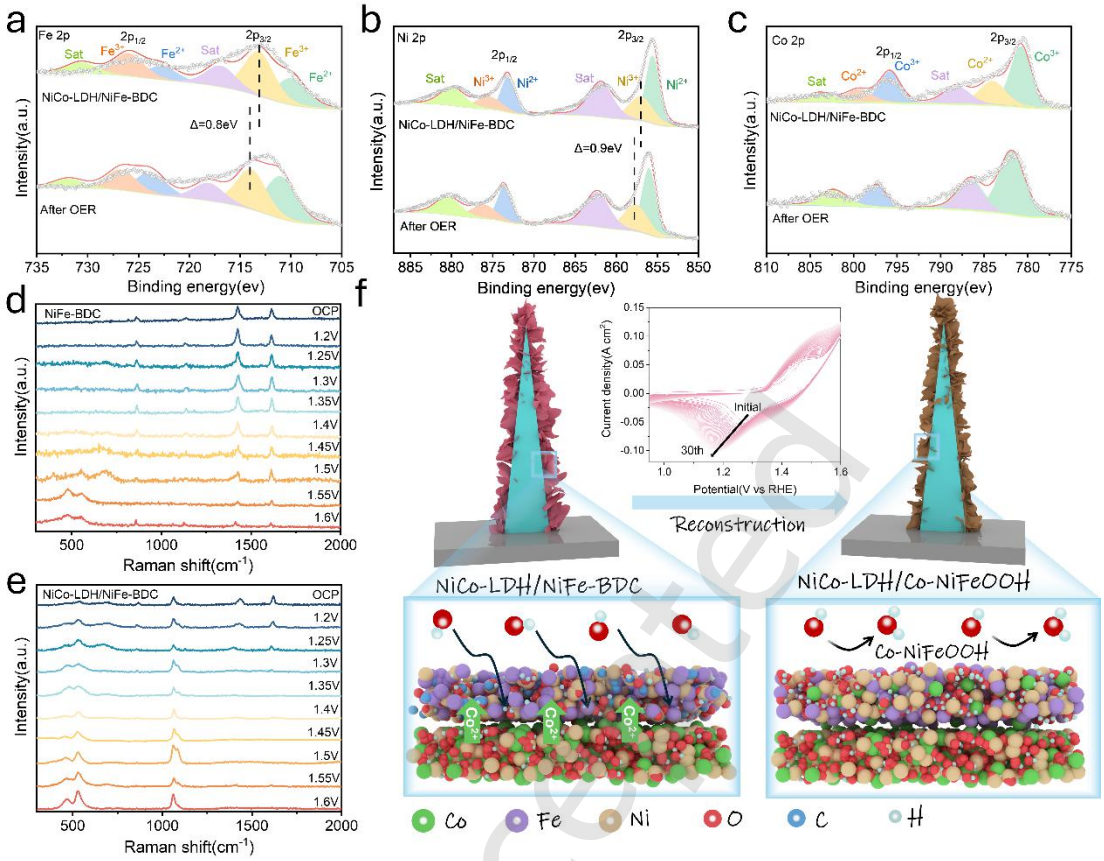

Fig. 2 Surface reconstruction of NiCo-LDH/NiFe-BDC. High-resolution XPS spectra of (a) Fe 2p, (b) Ni 2p, (c) Co 2p for NiCo-LDH/NiFe-BDC before and after OER. *In-situ* Raman spectra of (d) NiFe-BDC, (e) NiCo-LDH@NiFe-BDC. (f) Schematic illustration of the structural evolution.

In-situ Raman measurements were conducted to capture the active catalytic species and possible reaction intermediates (Fig. S13). As illustrated in **Fig. 2d, e**, under open circuit potential (OCP) conditions, the characteristic peaks are consistent with the *ex-situ* Raman spectra of NiFe-BDC and NiCo-LDH/NiFe-BDC. As the applied potential increased from 1.2 V to 1.6 V (vs. Hg/HgO), the intensities of characteristic peaks in the range of 300-700 cm^{-1} were enhanced, in which the peaks at ~466 and ~532 cm^{-1} can be assigned to the bending vibration (E_g) and the stretching vibration (A_{1g}) of NiOOH, respectively, while the weak and broad peak around 690 cm^{-1} are ascribed to Fe−O species, indicating the generation of NiFeOOH upon the surface reconstruction.[32] Simultaneously, the organic ligands are leached from the

MOF lattice to release uncoordinated carboxylate. Notably, for NiCo-LDH/NiFe-BDC, the reconstruction occurred at 1.3 V, which is lower than that of NiFe-BDC (1.45 V). This indicates that the low-valence metal sites in the optimal catalyst can be rapidly oxidized, which is favorable for activating lattice oxygen.

By comparing the intensities of E_g and A_{1g} peaks, it is convenient to distinguish whether NiFeOOH belongs to the β-phase or γ-phase (Fig. S14). When the peak intensity of E_g exceeds that of A_{1g} peak, it can be determined as γ-NiFeOOH, otherwise, it is β-NiFeOOH.[33] In the case of NiCo-LDH/NiFe-BDC, the intensity of E_g peak is weaker than that of the A_{1g} peak across all potentials, with a calculated $I_{E_g}/I_{A_{1g}}$ value of 0.67 (Figs. S15), while the $I_{E_g}/I_{A_{1g}}$ is estimated to be 2.33 for NiFe-BDC. This suggests that Co diffusion lowers the reconstruction voltage of catalyst and induces the phase transformation from γ-NiOOH to β-NiOOH.[34] Based on above characterizations, the NiCo-LDH nanorods not only serve as a structural skeleton, expanding the surface area to facilitate electrolyte penetration and OH^- adsorption, but also realize the Co diffusion through the hierarchical structure, accelerating the fast formation of Co-NiFeOOH (**Fig. 2f**). To further understand the valence and coordination states of Fe in NiFe-BDC and NiCo-LDH/NiFe-BDC, the Fe K-edge X-ray absorption near-edge structure (XANES) spectra were collected (Fig. S16a). The near-edge absorption position of Fe in NiCo-LDH/NiFe-BDC is very close to that of NiFe-BDC and higher than that of FeO. In the X-ray absorption fine structure (EXAFS) spectra (Fig. S16b), the peak at approximately ~0.89 Å can be attributed to Fe–O coordination. Notably, compared with pristine NiFe-BDC, the diffusion of Co causes a slightly shift toward a higher R value (0.89 Å → 0.96 Å), which is attributed to the elongation of Fe–O bonds. The weakened Fe–O coordination lowers the energy barrier required for bond cleavage, thereby facilitating structural reconstruction.

As a proof of concept, the electrochemical features of as-prepared samples were evaluated in 1 M KOH by using a standard three-electrode system. The consecutive

CV curves were recorded at a scan rate of 2 mV/s (Fig. S17a). NiCo-LDH/NiFe-BDC exhibits two anodic peaks, namely A_1 and A_2, at 1.35 V and 1.49 V *vs.* RHE, respectively. The A_1 peak is attributed to the oxidation of Co^{2+} to Co^{3+}, and its presence also indicates the diffusion of Co from NiCo-LDH to NiFe-BDC. The A_2 peak is considered as the oxidation of Co^{3+}, Fe^{3+}, and Ni^{3+} to higher oxidation state (Co^{4+}/Fe^{4+}/ Ni^{4+}),[35, 36] marking the initiation of the OER process. Besides, two cathodic peaks, C_1 and C_2, are observed when the potential shifts negatively. NiFe-BDC only shows the A_2 peak at a higher potential (1.57 V *vs.* RHE) accompanied with C_2 peak upon the negative potential scan (Fig. S17b). The reversible redox behavior of NiCo-LDH/NiFe-BDC is enhanced with the presence of Co element.[37]

The electrochemical OER performance of NiCo-LDH/NiFe-BDC was studied, and all polarization curves in this work were corrected with 95% iR compensation. The linear sweep voltammetry (LSV) curve of NiCo-LDH/NiFe-BDC exhibits a significantly enhance OER activity compared to NiFe-BDC, NiCo-LDH, and commercial RuO_2 (**Fig. 3a**). A Co-free control sample (NiFe-LDH/NiFe-BDC) was supplemented for comparison, and LSV curves show that the incorporation of Co effectively promotes the catalytic activity and decreases the reconstruction potential (Fig.S18). Achieving the current densities of 10, 100, and 500 mA cm^{-2}, NiCo-LDH/NiFe-BDC only requires overpotentials of 180, 255, and 300 mV, respectively, which are more exceptional than those of NiFe-BDC, NiCo-LDH, and RuO_2 (**Fig. 3b**). Compared to the other three catalysts, NiCo-LDH/NiFe-BDC also exhibits the lowest Tafel slope (19 mV dec^{-1}), while the other two catalysts show slopes of 29 and 69 mV dec^{-1}, respectively (**Fig. 3c**). Given the excellent alkaline OER activity, the catalytic performance was also investigated in alkaline seawater. The catalytic activity in alkaline seawater remains robust, and only slight decrease is observed in comparison to that in alkaline freshwater (Fig. S19) due to the corrosion effect of Cl^-.

The electrocatalytic active surface area (ECSA), which is proportional to the electrochemical double-layer capacitance (C_{dl}), is believed as a vital factor influcing catalytic activity. C_{dl} can be estimated by performing CV tests in the non-Faradic region at different scan rates (Fig. S20). As shown in **Fig. 3d**, the C_{dl} values of the NiCo-LDH/NiFe-BDC, NiFe-BDC, NiCo-LDH electrodes are calculated to be 79, 39, and 23 mF cm^{-2}, respectively. Thus, the calculated ECSA values follow the trend: NiCo-LDH/NiFe-BDC (197.5 cm^2) > NiFe-BDC (97.5 cm^2) > NiCo-LDH (57.5 cm^2), indicating the most abundant active sites on NiCo-LDH/NiFe-BDC. Electrochemical impedance spectroscopy (EIS) is a powerful tool for gaining insights into the OER kinetics. The recorded Nyquist plot data were fitted using the Randles equivalent circuit, where R_{ct} represents the charge transfer resistance. NiCo-LDH/NiFe-BDC exhibits the smallest R_{ct} of 1.2 Ω·cm^2 at a potential of 1.47 V *vs.* RHE (**Fig. 3e**), in comparison to those of NiFe-BDC (1.8 Ω·cm^2) and NiCo-LDH (>6 Ω·cm^2), manifesting its fastest charge transfer at the electrode-electrolyte interface (Table S2).

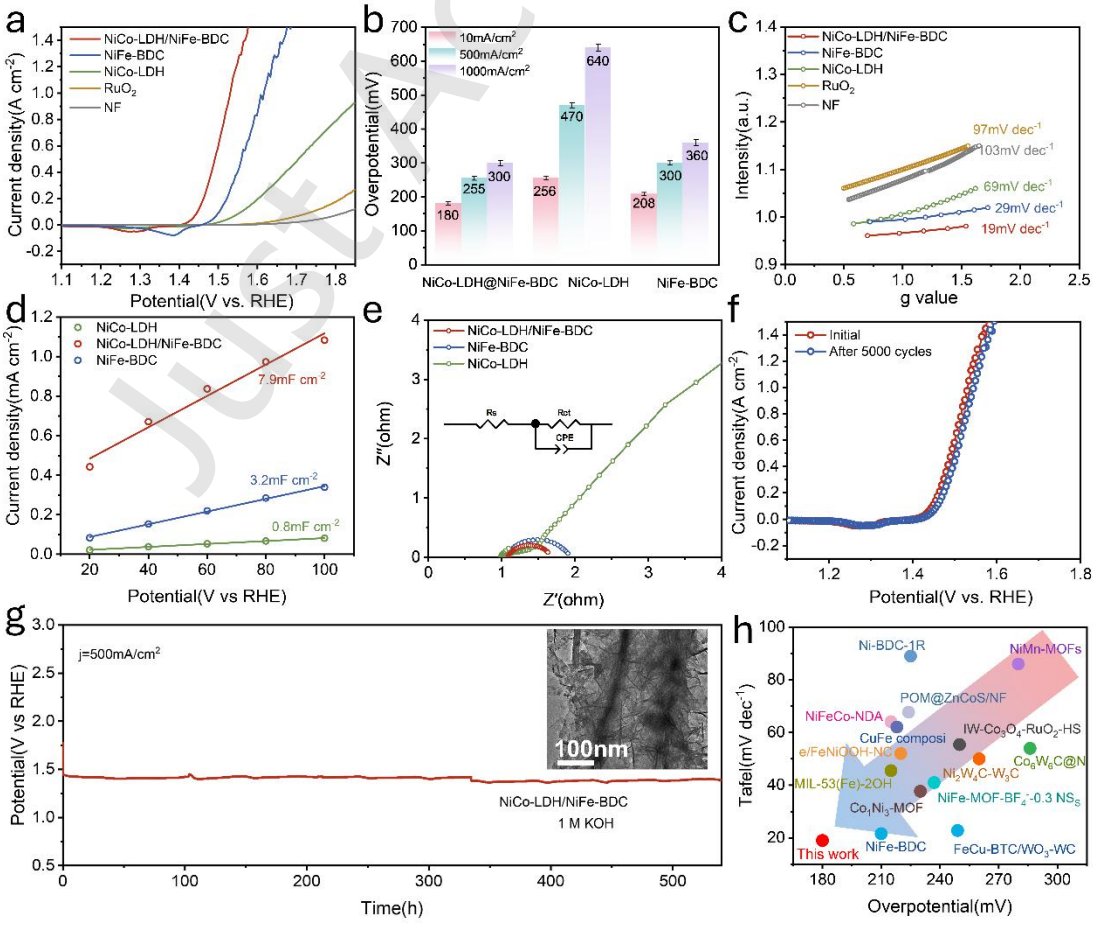

Fig. 3 Electrochemical OER performance. (a) OER polarization curves of NiCo-LDH/@NiFe-BDC, NiFe-BDC, NiFe-LDH, RuO_2, and NF in 1 M KOH. (b) Corresponding overpotentials of catalysts at 10, 500 and 1000 mA cm^{-2}. (c) Tafel slopes. (d) Double layer capacitors. (e) Nyquist plots. (f) LSV curves of NiCo-LDH/NiFe-BDC before and after 5000 CV cycles. (g) Chronoamperometric stability test. (h) Comparison of the reported overpotentials at 10 mA cm^{-2}.

The long-term stability is a key parameter to evaluate the feasibility of catalysts in practical applications. The cyclic durability was studied by conducting continuous CV at a scan rate of 100 mV s^{-1} in the potential range of 1.1 to 1.6 V *vs.* RHE (**Fig. 3f**). After 5000 CV cycles, only minor differences can be observed compared to the initial polarization curve. Additionally, the applied potential demonstrates no apparent attenuation (within 1% potential decrease) after a chronopotentiometry test at a constant current density of 500 mA cm^{-2} over 500 h (**Fig. 3g**). The hierarchical morphology can be well preserved as well. These results verify the extraordinary stability of NiCo-LDH/NiFe-BDC. Surprisingly, after continuous operation for 300 h in alkaline seawater, the performance also shows negligible degradation, further confirming the catalyst's excellent stability under high corrosive environment (Fig. S21). Owing to the excellent OER properties, our optimum catalyst surpasses almost all recently reported transition metal-based OER catalysts, including LOM-based catalysts (**Fig. 3h** and Table S3). In addition, after prolonged electrolysis, the XRD diffraction peaks exhibit a slight decrease in intensity (Fig. S22), indicating no significant structural degradation. Meanwhile, the XPS spectra show rare changes in chemical states of key metal elements (Fig. S23), suggesting that the catalyst surface maintains good chemical stability during long-term operation.

In practical applications, extensive gas bubbles are generated on the catalyst's surface at high current densities. These bubbles may hinder the diffusion of electrolytes and block the exposure of active sites. To study the characteristics of bubble desorption, we analyzed the release behavior of bubbles during water splitting

(Fig. S24). Obviously, the size of bubbles generated on the reconstructed NiCo-LDH/NiFe-BDC with an average diameter of 157 ± 31 μm is smaller than that on NiFe-BDC (177 ± 39 μm). The bubbles are easier to release on the optimum catalyst due to the unique nano/micro-structured super-aerophobic surface.

To elucidate the excellent OER performance of NiCo-LDH/NiFe-BDC, the OER pathway and mechanistic insights should be explored. Because the LOM pathway follows a nonconcerted proton-electron transfer process, it exhibits pH-dependent activity.[38] LSV curves were recorded at different pH values, as shown in **Fig. 4a**, the NiCo-LDH/NiFe-BDC electrode shows strong pH dependence. With the pH decreasing from 14.0 to 12.5, its OER activity declines significantly, while NiFe-BDC and NiCo-LDH exhibit minimal pH dependence (**Fig. 4b**). Upon the potential of 1.58 V *vs.* RHE, the logarithm of current density shows a linear relationship with the pH value, based on which the proton reaction orders on the RHE scale (ρ_{RHE}) are fitted to be 1.30, 1.11, and 0.87 for NiCo-LDH/NiFe-BDC, NiFe-BDC, and NiCo-LDH.[39] Above results demonstrates that the self-adaptive Co doping triggers the lattice oxygen during OER.[40, 41]

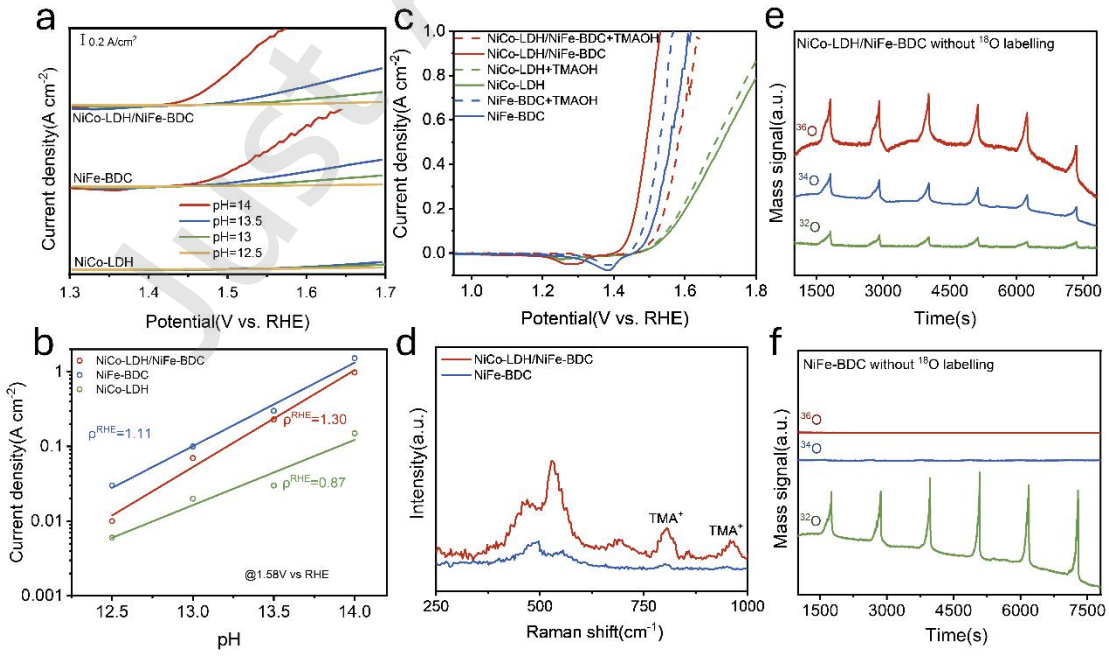

Fig. 4 Analysis of LOM pathway. (a) LSV plots measured with different pH values. (b) Current density plotted in log scale as a function of pH. (c) LSV plots measured in

KOH and TMAOH. (d) Raman spectra of NiCo-LDH/NiFe-BDC and NiFe-BDC in TMAOH. DEMS signals of (e) NiCo-LDH/NiFe-BDC, (f) NiFe-BDC.

Moreover, the direct O–O coupling is crucial to determine the LOM pathway, in which the superoxide (O_2^-) and peroxide (O_2^{2-}) species may be generated as negatively charged oxygen-containing intermediates. Therefore, it is essential to identify these charged intermediates during the OER process.[42] Based on this feature, tetramethylammonium hydroxide (TMAOH) can be used as a chemical probe, as its cation TMA^+ strongly binds with these negatively charged species, allowing it tracking the OER intermediates. As shown in **Fig. 4c**, compared with the system in 1 M KOH, the OER activity of NiCo-LDH/NiFe-BDC significantly decreases in 1 M TMAOH, whereas the activities of NiFe-BDC and NiCo-LDH remain almost unchanged. Additionally, as evidenced by the Raman spectra in **Fig. 4d**, the TMA^+ characteristic peaks appear at 813.2 and 983.5 cm^{-1} after the OER test in 1 M TMAOH, confirming interaction between TMA^+ and O_2^{2-} species on NiCo-LDH/NiFe-BDC. These findings provide indirect evidence for the reconstruction-mediated LOM pathway.

To provide direct evidence for the involvement of lattice oxygen, ^{18}O isotope labeling coupled with differential electrochemical mass spectrometry (DEMS) was carried out (**Fig. 4e, f**). NiCo-LDH/NiFe-BDC and NiFe-BDC anode underwent the CV pretreatment in 1 M KOH containing $H_2{}^{18}O$, which can induce the ^{18}O incorporation into the lattice. Subsequent CV measurements were performed in the electrolyte containing $H_2{}^{16}O$. Compared to the weak signals of NiFe-BDC, the periodic signals of the $^{18}O^{16}O$ (m/z = 34) and $^{18}O^{18}O$ (m/z = 36) for NiCo-LDH/NiFe-BDC remarkably enhance, confirming the involvement of lattice oxygen activated by Co doping.[43, 44]

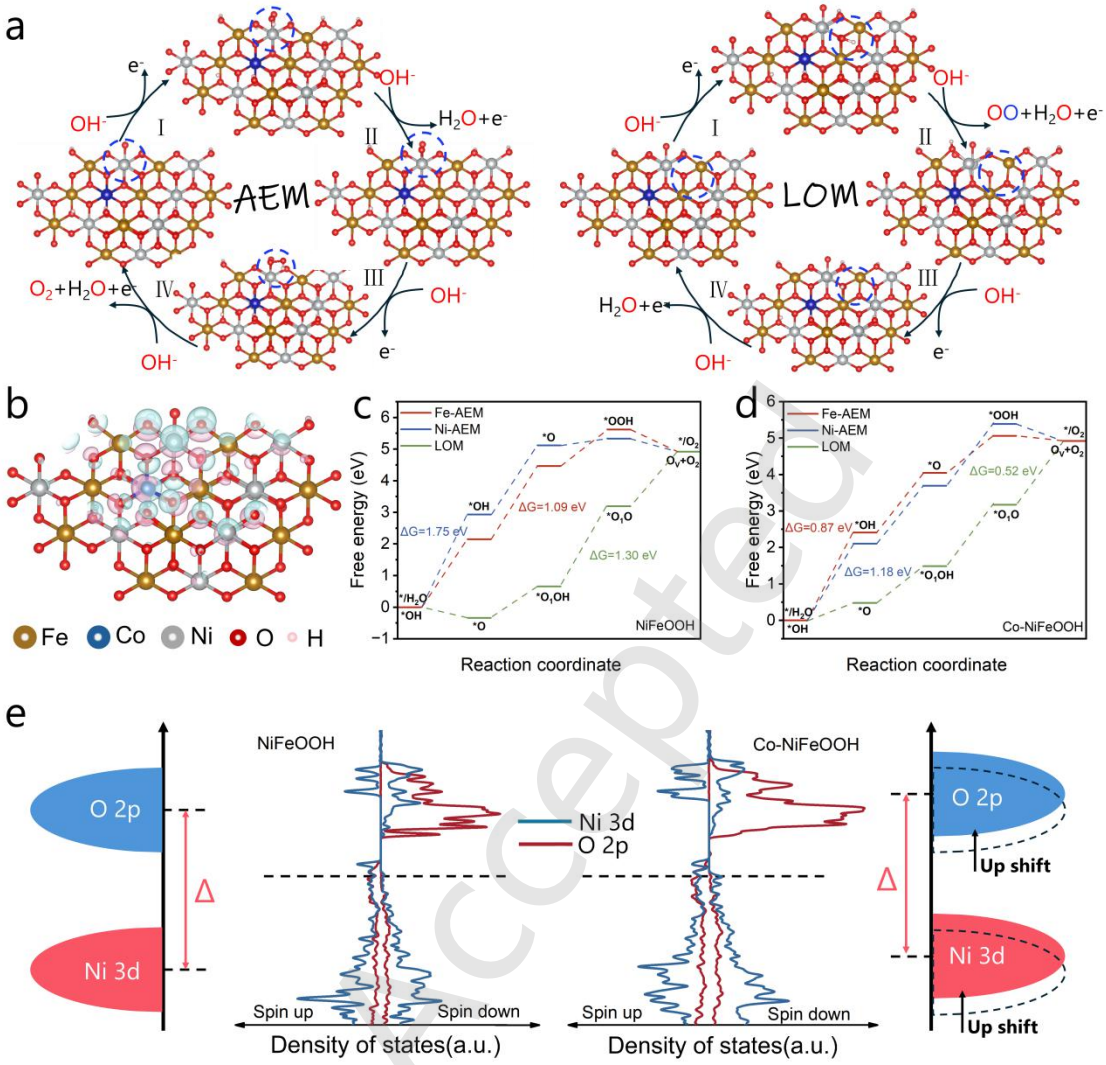

Fig. 5 DFT calculations for OER catalysts. (a) Schematic illustration of the possible LOM and AEM pathways on Co-NiFeOOH. (b) Differential charge density analysis of Co-NiFeOOH. Note: the pink and blue areas indicate electron accumulation and depletion, respectively. Free energy diagrams of OER steps on (c) NiFeOOH and (d) Co-NiFeOOH. (e) The schematic band diagrams and density of states of NiFeOOH and Co-NiFeOOH.

DFT calculations were performed to shed light on how Co incorporation boosted the OER performance of the reconstructed catalyst. The observed Co-NiFeOOH and NiFeOOH surfaces were utilized to study the reaction behavior of NiCo-LDH/NiFe-BDC and NiFe-BDC catalysts, respectively (Fig. S25). Additionally, the calculated formation energies imply the incorporated Co ions prefer to replace the

Ni ion at subsurface (Fig. S26). Four elementary steps are involved in both the AEM and LOM pathways (**Fig. 5a**). In this system, AEM involves four oxygen-containing intermediates: M–OH, M–O, M–OOH, and M–OO, while LOM proceeds through intermediates of O–M–OH, MOO, OO–M–□ , and M–OH, where M represents the metal site, O represents the lattice oxygen site and □ denotes oxygen vacancies. The differential charge density analysis clearly indicates the multi-metal interactions among Ni, Fe, and the incorporated Co atoms (**Fig. 5b**). Additionally, the incorporation of Co site, changes the spatial direction of O-2p to out-of-plane, which may modulate adsorption strength.

To elucidate the underlying mechanism, the Gibbs free energies of Co-NiFeOOH and NiFeOOH in each step under different reaction pathways were investigated by DFT calculations (Fig. S27 and S28).[45-47] The free energy diagram reveals that the OER steps of NiFeOOH follow a typical AEM pathway, where the rate-determining step (RDS) is the OH deprotonation at Fe site, which corresponds a limiting potential of 2.32 eV (**Fig. 5c**). This value is lower than that for LOM pathways involving bridging lattice oxygen (2.53 eV). For Co-NiFeOOH, the O_2 formation via the LOM route is the RDS, with a calculated ΔG of 1.75 eV (**Fig. 5d**). The oxygen from Ni–O–Fe bonding tends to be activated to form O_2 molecules. Thus, Co-NiFeOOH exhibits a higher OER activity due to a lower energy input required by the LOM pathway, in good agreement with the experimental results.

The electronic configurations of Co-NiFeOOH and NiFeOOH were also calculated (Fig. S29). Compared to NiFeOOH, the O 2p band center of Co-NiFeOOH shifts upwards relative to the Fermi level (E_F), facilitating the electron transfer from oxygen sites. This band shift enhances the hybridization between Ni 3d (Fe 3d) and O 2p orbitals, thereby activating the lattice oxygen and promoting the LOM pathway. Moreover, the d-band centers of Ni 3d and Fe 3d orbitals are upshifted from –2.94/–1.96 eV in NiFeOOH to –2.90/–1.87 eV in Co-NiFeOOH, respectively (**Fig. 5e** and S30).[48, 49] The resulting electron-rich characters of the metal sites can

improve their redox ability and facilitate electron transfer between the metal atoms and adsorbates,[50] thereby reducing the energy barrier for RDS.

Conclusion

In conclusion, we innovatively design the hierarchical NiCo-LDH/NiFe-BDC nano-heterojunction material as a pre-catalyst, which promotes its surface reconstruction with the fast Co ions diffusion from the LDH-core to the MOF-shell. As a result, the transformation of NiFeOOH from γ-phase to β-phase is induced and the reconstruction potential is reduced from 1.5 V to 1.3 V. The catalyst exhibits superior alkaline OER activity with low overpotentials of 180 mV and 255 mV at 10 and 500 mA cm^{-2}, respectively, with a Tafel slope of only 19 mV dec^{-1}. In addition, negligible current density loss can be observed at 500 mA cm^{-2} after 500-h continuous operation. Experimental results combined with theoretical calculations suggest that active Co incorporated NiFeOOH effectively triggers the participation of lattice oxygen from the Ni–O–Fe bonding. This work emphasizes the unique reconstruction mediated lattice oxygen mechanism on MOF/LDH pre-catalysts, which can potentially guide the design of OER electrocatalysts and regulation of their reaction mechanisms.

Data Availability Statement

The data supporting this article has been included as part of the ESI.

Conflict of Interest

There are no conflicts to declare.

Acknowledgements

This work was funded by the National Key Research and Development Program of China (2022YFB3803600), the National Natural Science Foundation of China

(22368050, 22378346), the Key Research and Development Program of Yunnan Province (202302AF080002), the Yunnan Basic Applied Research Project (202401AU070229, 202401AT070460), the Scientific Research Fund Project of Yunnan Education Department (2024J0013, 2024J0014), the Open Project of Yunnan Precious Metals Laboratory Co., Ltd (YPML-20240502008), the Science and Technology Development Fund (FDCT) from Macau SAR (0050/2023/RIB2). Authors thank the Shiyanjia Lab (www.shiyanjia.com), the Electron Microscopy Center, the Advanced Computing Center, and the Advanced Analysis and Measurement Center of Yunnan University for the sample testing and computational services.

References

[1] Yue, K.;Lu, R.;Gao, M.;Song, F.;Dai, Y.;Xia, C.;Mei, B.;Dong, H.;Qi, R.;Zhang, D.;Zhang, J.;Wang, Z.;Huang, F.;Xia, B. Y.; Yan, Y. Polyoxometalated metal-organic framework superstructure for stable water oxidation. *Science* **2025**, *388*, 430–436.

[2] Li, H.;Lin, Y.;Duan, J.;Wen, Q.;Liu, Y.; Zhai, T. Stability of electrocatalytic OER: from principle to application. *Chem. Soc. Rev.* **2024**, *53*, 10709–10740.

[3] Ren, G.;Zhou, M.;Hu, P.;Chen, J. F.; Wang, H. Bubble-water/catalyst triphase interface microenvironment accelerates photocatalytic OER via optimizing semi-hydrophobic OH radical. *Nature Communications* **2024**, *15*, 2346.

[4] Zhang, Y.;Liao, L.;Zhou, H.;Qi, Y.;Sun, J.;Zhang, Y.;Zhou, Q.;Wang, Y.;Tang, D.; Yu, F. Visualizing dynamic competitive reconstruction of trimetallic hybrid catalysts for stable hybrid water electrolysis at large current density. *Energ Environ Sci* **2025**, 10.1039/D5EE00172B.

[5] Xie, X.;Du, L.;Yan, L.;Park, S.;Qiu, Y.;Sokolowski, J.;Wang, W.; Shao, Y. Oxygen Evolution Reaction in Alkaline Environment: Material Challenges and Solutions. *Adv Funct Mater* **2022**, *32*, 2110036.

[6] Zhang, Z.;Lu, S.;Zhu, M.;Wang, F.;Yang, K.;Dong, B.;Yao, Q.; Hu, W. Enhancing Water Oxidation Performance of Transition Metal Oxides by Atomically Precise Heteroatom Doping. *Journal of the American Chemical Society* **2025**, *147*, 22806–22817.

[7] Jiang, Q.;Wang, S.;Zhang, C.;Sheng, Z.;Zhang, H.;Feng, R.;Ni, Y.;Tang, X.;Gu, Y.;Zhou, X.;Lee, S.;Zhang, D.; Song, F. Active oxygen species mediate the iron-promoting electrocatalysis of oxygen evolution reaction on metal oxyhydroxides. *Nat Commun* **2023**, *14*, 6826.

[8] Liu, H.;Liu, X.;Sun, A.;Xuan, C.;Ma, Y.;Zhang, Z.;Li, H.;Wu, Z.;Ma, T.; Wang, J. Enhancing Oxygen Evolution Electrocatalysis in Heazlewoodite: Unveiling the Critical Role of Entropy Levels and Surface Reconstruction.

Adv. Mater. **2025**, *37*, 2501186.

[9] Zhang, C.;Wu, Y.;Li, D.; Jiang, H.-L. Recent advances in MOF composites for photocatalysis. *Chemical Science* **2025**, *16*, 13149–13172.

[10] Zhao, J.;Guo, Y.;Zhang, Z.;Zhang, X.;Ji, Q.;Zhang, H.;Song, Z.;Liu, D.;Zeng, J.;Chuang, C.;Zhang, E.;Wang, Y.;Hu, G.;Mushtaq, M. A.;Raza, W.;Cai, X.; Ciucci, F. Out-of-plane coordination of iridium single atoms with organic molecules and cobalt–iron hydroxides to boost oxygen evolution reaction. *Nature Nanotechnology* **2024**, *20*, 57–66.

[11] Li, Z.;Lin, G.;Wang, L.;Lee, H.;Du, J.;Tang, T.;Ding, G.;Ren, R.;Li, W.;Cao, X.;Ding, S.;Ye, W.;Yang, W.; Sun, L. Seed-assisted formation of NiFe anode catalysts for anion exchange membrane water electrolysis at industrial-scale current density. *Nature Catalysis* **2024**, *7*, 944–952.

[12] Cai, S.;Wang, Q.;Zhang, N.;Chen, C.;Zhang, H.;Feng, Y.;Duan, L.;Cheng, Y.;Meng, Z.;Li, H.; Wu, J. Recent Progress in Halogen-Doped Single-Atom Catalysts for Electrochemical Reactions. *Carbon Neutralization* **2025**, *4*, e193.

[13] Su, Q.;Liu, Q.;Wang, P.;Ding, J.;Cheng, W.; Huang, Y. Fe doping regulates the surface reconstruction and activates lattice oxygen of NiCr LDH for water oxidation. *Chem. Eng. J.* **2024**, *483*, 149383.

[14] Yue, Y.;Zhong, X.;Sun, M.;Du, J.;Gao, W.;Hu, W.;Zhao, C.;Li, J.;Huang, B.;Li, Z.; Li, C. Fluorine Engineering Induces Phase Transformation in $NiCo_2O_4$ for Enhanced Active Motifs Formation in Oxygen Evolution Reaction. *Adv Mater* **2025**, *37*, 2418058.

[15] Li, X.;Deng, C.;Kong, Y.;Huo, Q.;Mi, L.;Sun, J.;Cao, J.;Shao, J.;Chen, X.;Zhou, W.;Lv, M.;Chai, X.;Yang, H.;Hu, Q.; He, C. Unlocking the Transition of Electrochemical Water Oxidation Mechanism Induced by Heteroatom Doping. *Angew. Chem. Int. Ed.* **2023**, *62*, e202309732.

[16] Wang, J.;Xing, Z.;Kang, R.;Zheng, Y.;Zhang, Z.;Ma, T.;Wang, Y.;Yin, B.;Liao, Y.;Li, L.;Cheng, C.; Li, S. Metal Nitride Controlled Atomic Doping

of Mo^{x+} in NiFe (Oxy)Hydroxide to Trigger Lattice Oxygen-Mediated Mechanism for Superior Oxygen Evolution. *Adv. Funct. Mater.* **2025**, *35*, 2418439.

[17] Zhang, T.;Zhao, H.-F.;Chen, Z.-J.;Yang, Q.;Gao, N.;Li, L.;Luo, N.;Zheng, J.;Bao, S.-D.;Peng, J.;Peng, X.;Liu, X.-W.; Yu, H.-B. High-entropy alloy enables multi-path electron synergism and lattice oxygen activation for enhanced oxygen evolution activity. *Nature Communications* **2025**, *16*, 3327.

[18] Yin, H.;Lin, Z.;Wang, L.;Huang, Y.;Isimjan, T. T.; Yang, X. Leveraging ligand push-pull effects in Ni-based MOFs for optimized lattice oxygen activation and superior water oxidation. *Applied Catalysis B: Environment and Energy* **2025**, *378*, 125610.

[19] Gu, Z.;Le, J.;Wei, H.;Sun, Z.;Hafez, M. E.; Ma, W. Unveiling the intrinsic properties of single NiZnFeOx entity for promoting electrocatalytic oxygen evolution. *Chinese Chem Lett* **2024**, *35*, 108849.

[20] Liu, T.;Lu, J.;Chen, Z.;Luo, Z.;Ren, Y.;Zhuge, X.;Luo, K.;Ren, G.;Lei, W.; Liu, D. Advances, mechanisms and applications in oxygen evolution electrocatalysis of gold-driven. *Chem. Eng. J.* **2024**, *496*, 153719.

[21] Zhao, J. W.;Yue, K.;Wu, L.;Yang, J.;Luan, D.;Zhang, X.; Lou, X. W. Surface Transformation in Lanthanum Nickelate for Enhanced Oxygen Evolution Catalysis. *Angew. Chem. Int. Ed.* **2025**, *64*, e202507144.

[22] Liu, Q.;Fu, T.;Xiao, H.;Yu, Y.;Che, Z.;Zhang, Y.;Chen, A.;Li, M.; Liu, T. Constructing the Ni4N/Ni3N Heterointerface of the Bicontinuous Ni4N/Ni3N/NiO/CFs Catalyst With Pore Connectivity Effects for Electrocatalytic Hydrogen Generation. *Carbon Neutralization* **2025**, *4*, e70024.

[23] Qiu, L.;Dong, A.;Yan, P.;Lin, Y.; Yu, X.-Y. Distinctive Plasma Engineering Ensuring Deep Reconstruction of Heterostructured Ni_2P/Fe_2P Into Metal Oxyhydroxides With Activated Lattice Oxygen for Water Oxidation at

Industrial Current Density. *Adv Funct Mater* **2025**, *n/a*, e08353.

[24] Mattioli, G.; Guidoni, L. Multiple Reaction Pathways for Oxygen Evolution as a Key Factor for the Catalytic Activity of Nickel–Iron (Oxy)Hydroxides. *Journal of the American Chemical Society* **2025**, *147*, 6450–6463.

[25] Wu, Z.-P.;Zuo, S.;Pei, Z.;Zhang, J.;Zheng, L.;Luan, D.;Zhang, H.; Lou, X. W. Operando unveiling the activity origin via preferential structural evolution in Ni-Fe (oxy)phosphides for efficient oxygen evolution. *Sci Adv*, *11*, eadu5370.

[26] Zhang, L.;Li, J.;Hu, M.;Xu, Y.;Xiong, X.; Jin, Z. MOF-derived beaded stream-like nitrogen and phosphorus-codoped carbon-coated Fe_3O_4 nanocomposites via lattice-oxygen-mediated mechanism for efficient water oxidation. *Chinese Chem Lett* **2025**, *36*, 111123.

[27] Qian, Z.-X.;Liang, G.-H.;Shen, L.-F.;Zhang, G.;Zheng, S.;Tian, J.-H.;Li, J.-F.; Zhang, H. Phase Engineering Facilitates O–O Coupling via Lattice Oxygen Mechanism for Enhanced Oxygen Evolution on Nickel–Iron Phosphide. *Journal of the American Chemical Society* **2024**, *147*, 1334–1343.

[28] Na, G.;Zheng, H.;Chen, M.;Sun, H.;Zhou, T.;Wu, Y.;Li, D.;Lu, Q.;Chen, Y.;Zhao, J.;Zhang, Y.;He, T.;Xiao, B.;Zhang, J.;Liu, F.;Cui, H.; Liu, Q. In-situ synthesis to promote surface reconstruction of metal–organic frameworks for high-performance water/seawater oxidation. *J Colloid Interf Sci* **2025**, *678*, 795–805.

[29] Wang, H.;Zhai, T.;Wu, Y.;Zhou, T.;Zhou, B.;Shang, C.; Guo, Z. High-Valence Oxides for High Performance Oxygen Evolution Electrocatalysis. *Adv Sci* **2023**, *10*, 2301706.

[30] Shu, W.;Le, F.;Yao, H.;Hu, P.;Yang, X.; Jia, W. Tailoring active sites in trimetallic conductive metal–organic frameworks for highly efficient water splitting. *Journal of Materials Chemistry A* **2025**, *13*, 13532–13541.

[31] Na, G.;Zheng, H.;Chen, M.;Sun, H.;Wu, Y.;Li, D.;Chen, Y.;Zhao, B.;Zhao, B.;Zhou, T.;He, T.;Zhang, Y.;Zhao, J.;Zhang, Y.;Zhang, J.;Liu, F.;Cui, H.; Liu,

Q. In-situ Pt reduction induced topological transformation of NiFe-MOF for industrial seawater splitting. *Chinese Journal of Catalysis* **2025**, *72*, 211–221.

[32] Ke, J.;Zhang, J.;Zhang, L.;He, S.;Zhong, C.;Du, L.;Song, H.;Fang, X.;Zhang, Z.; Cui, Z. Role of High-Valence Metal Dissolution in Oxygen Evolution Kinetics of the Advanced FeNiOx Catalysts. *Acs Catal* **2024**, *14*, 16363–16373.

[33] He, X.;Yao, Y.;Zhang, L.;Wang, H.;Tang, H.;Jiang, W.;Ren, Y.;Nan, J.;Luo, Y.;Wu, T.;Luo, F.;Tang, B.; Sun, X. Hexafluorophosphate additive enables durable seawater oxidation at ampere-level current density. *Nature Communications* **2025**, *16*.

[34] Li, M.;Wang, X.;Liu, K.;Sun, H.;Sun, D.;Huang, K.;Tang, Y.;Xing, W.;Li, H.; Fu, G. Reinforcing Co O Covalency via Ce(4f)─O(2p)─Co(3d) Gradient Orbital Coupling for High-Efficiency Oxygen Evolution. *Adv. Mater.* **2023**, *35*, 2302462.

[35] Xiao, Z.;Huang, Y.-C.;Dong, C.-L.;Xie, C.;Liu, Z.;Du, S.;Chen, W.;Yan, D.;Tao, L.;Shu, Z.;Zhang, G.;Duan, H.;Wang, Y.;Zou, Y.;Chen, R.; Wang, S. Operando Identification of the Dynamic Behavior of Oxygen Vacancy-Rich Co_3O_4 for Oxygen Evolution Reaction. *Journal of the American Chemical Society* **2020**, *142*, 12087–12095.

[36] Wu, T.;Sun, S.;Song, J.;Xi, S.;Du, Y.;Chen, B.;Sasangka, W. A.;Liao, H.;Gan, C. L.;Scherer, G. G.;Zeng, L.;Wang, H.;Li, H.;Grimaud, A.; Xu, Z. J. Iron-facilitated dynamic active-site generation on spinel $CoAl_2O_4$ with self-termination of surface reconstruction for water oxidation. *Nature Catalysis* **2019**, *2*, 763–772.

[37] Wang, X.;Hu, J.;Lu, T.;Wang, H.;Sun, D.;Tang, Y.;Li, H.; Fu, G. Importing Atomic Rare‐Earth Sites to Activate Lattice Oxygen of Spinel Oxides for Electrocatalytic Oxygen Evolution. *Angew. Chem. Int. Ed.* **2024**, *64*.

[38] Pan, Y.;Wang, Z.;Wang, K.;Ye, Q.;Shen, B.;Yang, F.; Cheng, Y. Dual Doping

of B and Fe Activated Lattice Oxygen Participation for Enhanced Oxygen Evolution Reaction Activity in Alkaline Freshwater and Seawater. *Adv Funct Mater* **2024**, *34*, 2402264.

[39] Xu, X.;Pan, Y.;Zhong, Y.;Shi, C.;Guan, D.;Ge, L.;Hu, Z.;Chin, Y.-Y.;Lin, H.-J.;Chen, C.-T.;Wang, H.;Jiang, S. P.; Shao, Z. New Undisputed Evidence and Strategy for Enhanced Lattice-Oxygen Participation of Perovskite Electrocatalyst through Cation Deficiency Manipulation. *Adv Sci* **2022**, *9*, 2200530.

[40] Zhao, J.-W.;Shi, Z.-X.;Li, C.-F.;Ren, Q.; Li, G.-R. Regulation of Perovskite Surface Stability on the Electrocatalysis of Oxygen Evolution Reaction. *ACS Materials Letters* **2021**, *3*, 721–737.

[41] Yang, C.;Batuk, M.;Jacquet, Q.;Rousse, G.;Yin, W.;Zhang, L.;Hadermann, J.;Abakumov, A. M.;Cibin, G.;Chadwick, A.;Tarascon, J.-M.; Grimaud, A. Revealing pH-Dependent Activities and Surface Instabilities for Ni-Based Electrocatalysts during the Oxygen Evolution Reaction. *ACS Energy Letters* **2018**, *3*, 2884–2890.

[42] Wang, F.;Feng, L.;Zhang, M.; Cong, H. Engineering oxygen nonbonding states in high entropy hydroxides for scalable water oxidation. *Nat Commun* **2025**, *16*, 6624.

[43] Zhao, J.-W.;Yue, K.;Zhang, H.;Wei, S.-Y.;Zhu, J.;Wang, D.;Chen, J.;Fominski, V. Y.; Li, G.-R. The formation of unsaturated IrOx in $SrIrO_3$ by cobalt-doping for acidic oxygen evolution reaction. *Nature Communications* **2024**, *15*, 2928.

[44] Guan Xu, H.;Zhu, C.;Yang Lin, H.;Kai Liu, J.;Xiao Wu, Y.;Qin Fu, H.;Yu Zhang, X.;Mao, F.;Yang Yuan, H.;Sun, C.;Fei Liu, P.; Gui Yang, H. Oxygen Plasma Triggered Co−O−Fe Motif in Prussian Blue Analogue for Efficient and Robust Alkaline Water Oxidation. *Angewandte Chemie International Edition* **2025**, *64*, e202415423.

[45] Chen, Y.;Xu, J.;Chen, Y.;Wang, L.;Jiang, S.;Xie, Z.-H.;Zhang, T.;Munroe, P.; Peng, S. Rapid Defect Engineering in FeCoNi/$FeAl_2O_4$ Hybrid for Enhanced Oxygen Evolution Catalysis: A Pathway to High-Performance Electrocatalysts. *Angew. Chem. Int. Ed.* **2024**, *63*, e202405372.

[46] Wang, Y.;Ge, X.;Lu, Q.;Bai, W.;Ye, C.;Shao, Z.; Bu, Y. Accelerated deprotonation with a hydroxy-silicon alkali solid for rechargeable zinc-air batteries. *Nature Communications* **2023**, *14*, 6968.

[47] Huang, Z.-F.;Xi, S.;Song, J.;Dou, S.;Li, X.;Du, Y.;Diao, C.;Xu, Z. J.; Wang, X. Tuning of lattice oxygen reactivity and scaling relation to construct better oxygen evolution electrocatalyst. *Nature Communications* **2021**, *12*, 3992.

[48] Tang, L.;Yang, Y.;Guo, H.;Wang, Y.;Wang, M.;Liu, Z.;Yang, G.;Fu, X.;Luo, Y.;Jiang, C.;Zhao, Y.;Shao, Z.; Sun, Y. High Configuration Entropy Activated Lattice Oxygen for O_2 Formation on Perovskite Electrocatalyst. *Adv. Funct. Mater.* **2022**, *32*, 2112157.

[49] Xiao, K.;Wang, Y.;Wu, P.;Hou, L.; Liu, Z.-Q. Activating Lattice Oxygen in Spinel $ZnCo_2O_4$ through Filling Oxygen Vacancies with Fluorine for Electrocatalytic Oxygen Evolution. *Angew. Chem. Int. Ed.* **2023**, *62*, e202301408.

[50] Song, J.;Wei, C.;Huang, Z. F.;Liu, C.;Zeng, L.;Wang, X.; Xu, Z. J. A review on fundamentals for designing oxygen evolution electrocatalysts. *Chem. Soc. Rev.* **2020**, *49*, 2196–2214.

Electronic Supplementary Material

Reconstruction mediated lattice oxygen mechanism on hierarchical LDH/MOF nanoarrays for efficient oxygen evolution

Guohao Na[1,§], *Mingpeng Chen*[1,§,*], *Yuewen Wu*[1], *Huachuan Sun*[1], *Dequan Li*[1], *Tong Zhou*[1], *Nan Yang*[1], *Fangyue Chen*[1], *Yun Chen*[1], *Yumin Zhang*[1], *Jin Zhang*[1], *Di Liu*[2,*],, *Hui Pan*[2], *Hao Cui*[3], and *Qingju Liu*[1,*]

[1] Yunnan Key Laboratory for Micro/Nano Materials & Technology, School of Materials and Energy, Yunnan University, Kunming 650091, China

[2] Institute of Applied Physics and Materials Engineering (IAPME), University of Macau, Macao 999078, China

[3] Yunnan Precious Metals Laboratory Co., Ltd., Kunming 650106, China

[§] Guohao Na and Mingpeng Chen contributed equally to this work.

Address correspondence to Mingpeng Chen, mpchen@ynu.edu.cn; Di Liu, diliu@um.edu.mo; Qingju Liu, qjliu@ynu.edu.cn

Supporting information to https://doi.org/10.26599/NR.2026.94908945

Experimental section

Materials

Nickel foam (NF, thickness: 1.5 mm) was acquired from Kunshan Guangjiayuan New Material Co., Ltd. Nickle nitrate hexahydrate ($Ni(NO_3)_2 \cdot 6H_2O$, ≥98%) and hydrochloric acid (HCl) were purchased from Tianjin Windship Chemical Reagent Technology Co., Ltd. Iron(III) nitrate nonahydrate ($Fe(NO_3)_3 \cdot 9H_2O$, ≥99.5%), cobalt(II) nitrate hexahydrate ($Co(NO_3)_2 \cdot 6H_2O$, ≥99%), ruthenium(IV) oxide (RuO_2, 99.9%), p-phthalic acid ($C_8H_6O_4$ (BDC), 99%), urea (CH_4N_2O, ≥99.5%), ammonium fluoride (NH_4F, ≥98%), N-N-dimethylformamide (DMF, 99.5%), and potassium hydroxide (KOH, 85%) were purchased from Aladdin. Nafion solution (5 wt.%) was bought from Sigma Aldrich Corporation. Heavy-oxygen water (H_2O^{18}, 97 at.%) was bought from Macklin Biochemical Co., Ltd.

Synthesis of NiFe-BDC, NiCo-LDH and NiFe-BDC/NiCo-LDH

Firstly, a piece of NF (2×3 cm^2) was subsequently cleaned in 1 M HCl, deionized (DI) water, and ethanol. Next, DMF (26 mL), ethanol (1.6 mL), and DI water (1.6 mL) were thoroughly mixed, followed by the addition of 200 mg $C_8H_6O_4$ and 1 mmol $Fe(NO_3)_3 \cdot 9H_2O$. The mixture was transferred into a stainless-steel autoclave and heated at 120℃ for 24 h. NiFe-BDC electrode was collected, cleaned, and air-dried.

NiCo-LDH was synthesized by a convenient hydrothermal method, where 10 mmol CH_4N_2O, 4 mmol NH_4F, and 2 mmol $Co(NO_3)_2 \cdot 6H_2O$ were added into DI water to form a homogeneous solution (30 mL), followed by pouring it into the autoclave and setting it in the oven at 120℃ for 12 h. Under hydrothermal conditions, the OH^- released from the hydrolysis of urea reacts with Ni^{2+} and Co^{2+} ions to form NiCo-LDH nanoarrays. The reaction equation is as follows:

$$Ni(NO_3)_2 \cdot 6H_2O + Co(NO_3)_2 \cdot 6H_2O + CO(NH_2)_2 \rightarrow \text{NiCo-LDH} \quad (1)$$

NiFe-MOF/NiCo-LDH electrode was obtained by in-situ growth of NiFe-BDC on the NiCo-LDH electrode. The synthetic process was similar to that of pristine

NiFe-BDC, except that extra $Ni(NO_3)_2 \cdot 6H_2O$ precursor was required.

Characterizations

Scanning electron microscopy (SEM, GeminiSEM 460), and transmission electron microscopy (TEM, JEM-2100) were conducted to characterize the morphology and structure of as-obtained catalysts. Aberration-corrected high-angle annular dark-field scanning transmission electron microscopy (HAADF-STEM) images were obtained on Thermofisher Spectra 300 equipped with a probe corrector. X-ray diffraction (XRD) data was recorded on an X-ray diffractometer (Rigaku TTR-III) with a Cu Kα source. X-Ray photoelectron spectroscopy (XPS, K-Alpha) tests were conducted using Al source radiation. In-situ and ex-situ Raman spectra were recorded using a LabRAM HR Evolution Raman spectrometer (HORIBA) with a laser excitation of 532 nm. The X-ray absorption spectra (XAS) including XANES and EXAFS were collected on Rapid XAFS 2M.

Differential electrochemical mass spectrometric measurements

In-situ differential electrochemical mass spectrometry (DEMS) experiments were performed in a dual layer flow cell provided by Linglu Instruments Co., Ltd. The sample was labeled with ^{18}O isotope by performing 30-cycle cyclic voltammetry (CV) in 1 M KOH containing $H_2{}^{18}O$. The labeled electrode was then immersed in 1 M KOH containing $H_2{}^{16}O$ during OER test.

The mass spectrometry signals corresponding to m/z = 32 ($^{16}O^{16}O$), 34 ($^{18}O^{16}O$), and 36 ($^{18}O^{18}O$) were recorded, and the intensity ratios were analyzed to determine the fraction of oxygen molecules originating from the lattice. The lattice oxygen contribution rate (R_{LOM}) was calculated using the following formula:

$$R_{\mathrm{LOM}} = \frac{2I_{34}+2I_{36}}{2I_{34}+2I_{36}+4I_{32}} \times 100\% \qquad (2)$$

where I_{32},I_{34},and $I_{36}$are the integrated peak intensities of the corresponding oxygen species. This method accounts for both singly and doubly labeled oxygen molecules, providing a quantitative estimation of lattice oxygen participation.

Electrochemical measurements

An EnergyLab XM potentiostat (Solartron Analytical) was utilized for electrochemical measurements in a conventional three-electrode system in 1 M KOH (pH=14.0). The as-obtained sample, carbon rod, and Hg/HgO were used as the working electrode (1×1 cm^2), counter electrode, and reference electrode, respectively. All recorded potentials were calibrated to the reversible hydrogen electrode (RHE) scale:

$$E_{\mathrm{RHE}} = E_{\mathrm{Hg/HgO}} + E^0_{\mathrm{Hg/HgO}} + 0.0592pH (E^0_{\mathrm{Hg/HgO}} = 0.098\mathrm{V}\ vs\ \mathrm{RHE}) \qquad (3)$$

Before OER test, the electrochemical activation was applied to catalysts through CV scans at a scan rate of 100 mV s^{-1}. The electrocatalytic activity was examined by linear sweep voltammetry (LSV) at a scan rate of 2 mV s^{-1} with an iR compensation of 95%. The Tafel slope was obtained by fitting the linear portion of the Tafel plots according to the following equation:

$$\eta = \mathrm{b}\log(j) + \mathrm{a} \qquad (4)$$

The EIS was recorded at an applied potential of 1.5 V vs. RHE from 100000 to 0.01Hz. Electrochemical double-layer capacitance (C_{dl}) can be determined by varing the CV scan rates (20, 40, 60, 80 and 100 mV·s^{-1}) in a non-Faradaic region (from 0.1 to 0.2 V *vs.* Hg/HgO). In order to reduce experimental errors, we conducted four repeated tests to record the electrochemical data and utilized their average value.

Computational details

Our first-principles calculations were carried out using the Vienna Ab initio Simulation Package within the framework of density functional theory (DFT)[1, 2] The projector augmented wave pseudo-potentials method[3] and Perdew–Burke–Ernzerhof (PBE) functional[4] under the generalized gradient approximation were applied. To describe localized d-electron interactions, PBE + U calculations were utilized with effective Hubbard U values of 3.3 eV, 4.3 eV, and 5.5 eV for Co, Fe, and Ni, respectively[5]. Pristine and Co-incorporated NiFeOOH were represented by (10-1) terminated slabs consisting of $2 \times \sqrt{3} \times 2$ primitive units to calculate the catalytic process. A vacuum region of 15 Å along the vertical direction was set to avoid interaction between repeating slabs. Plane-wave cutoff energy was

set to 400 eV, with convergence thresholds of 10^{-5} eV for energy and 0.03 eV/Å for force. Van der Waals corrections were applied via the DFT-D3 method[6]. The 2×2×1 and 3×3×1 Monkhorst-Pack[7] type *k*-point sampling were used for structure optimization and surface calculations, respectively. The top two layers and adsorbates were relaxed during optimization, with other layers fixed[8, 9]. The computational standard hydrogen electrode (SHE) model proposed by Nørskov et al[10] was employed to evaluate the free energy change of each elementary step of OER. According to this model, the proton-electron pair's free energy equals half the chemical potential of H_2 gas under SHE conditions[11]. The OER's 4-electron pathways in alkaline media can be given as follows:

$$* + OH^- \rightarrow *OH + e^- \quad (5)$$

$$*OH + OH^- \rightarrow *O + H_2O\ (l) + e^- \quad (6)$$

$$*O + OH^- \rightarrow *OOH + e^- \quad (7)$$

$$*OOH + OH^- \rightarrow * + O_2\ (g) + H_2O\ (l) + e^- \quad (8)$$

Therefore, the free-energy change of four reaction steps can be expressed as follows:

$$\Delta G_1 = G\ (*OH) + G\ (H_2)/2 + eU - G\ (*) - G\ (H_2O) \quad (9)$$

$$\Delta G_2 = G\ (*O) + G\ (H_2)/2 + eU - G\ (*OH) \quad (10)$$

$$\Delta G_3 = G\ (*OOH) + G\ (H_2)/2 + eU - G\ (*O) - G\ (H_2O) \quad (11)$$

$$\Delta G_4 = G\ (*) + G\ (H_2)/2 + eU + G\ (O_2) - G\ (*OOH) \quad (12)$$

where U is the potential measured against the normal hydrogen electrode under standard conditions[12, 13]. The theoretical overpotential for OER (η_{OER}) can be calculated by $\eta_{OER} = \max[\Delta G_1, \Delta G_2, \Delta G_3, \Delta G_4]/e - U_{eq}$, where U_{eq} is the equilibrium potential[14].

The formation energy for the replacement was calculated using Equation (13):

$$E_F = E\ (bulk + Co) + E\ (Ni / Fe) - E(bulk) - E(Co) \quad (13)$$

where E (bulk) and E (bulk + Co) are the total energies of pure and Co-incorporated NiFeOOH, respectively. E (Co) and E (Ni / Fe) are the chemical potentials of Co and Ni/Fe, respectively, calculated from the energies of metal bulks.

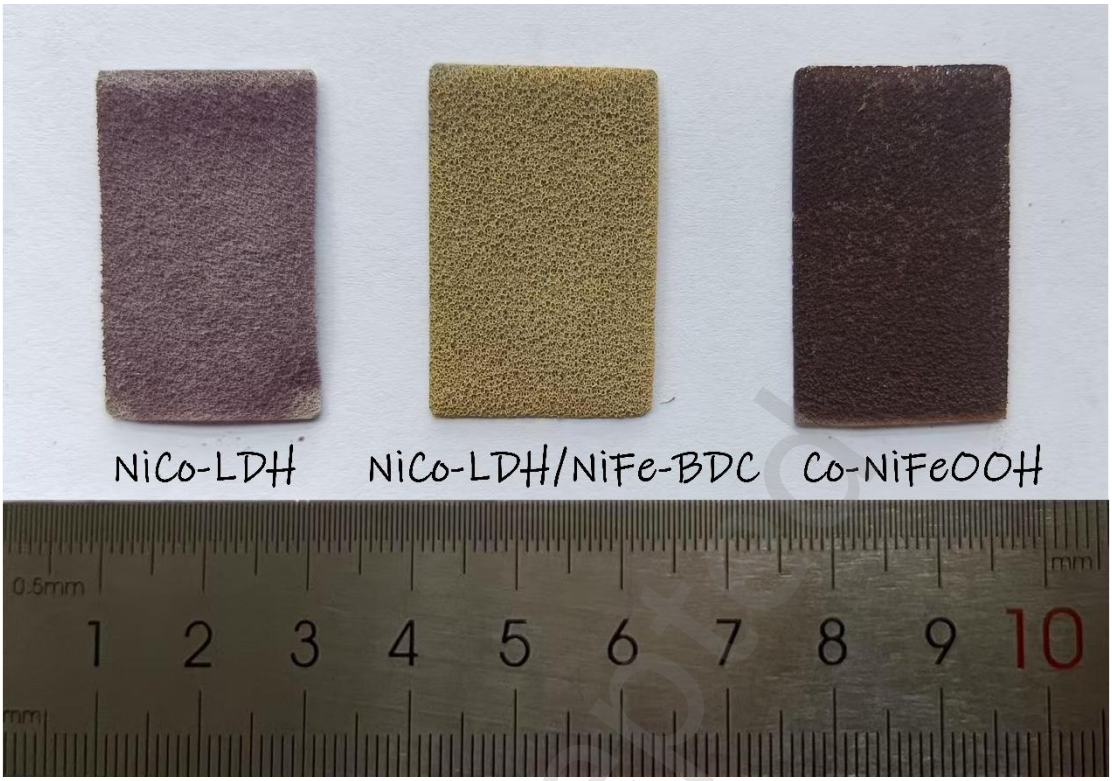

Fig. S1 Digital photograph of as-prepared samples.

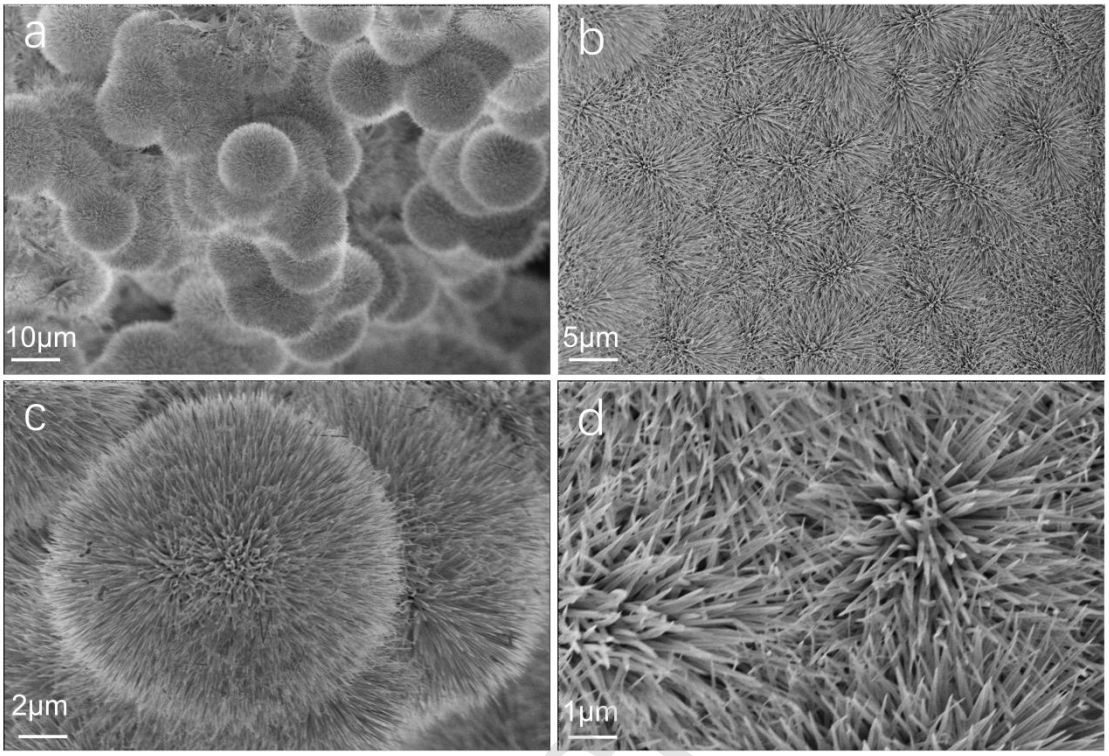

Fig. S2 SEM images of NiCo-LDH at various magnifications.

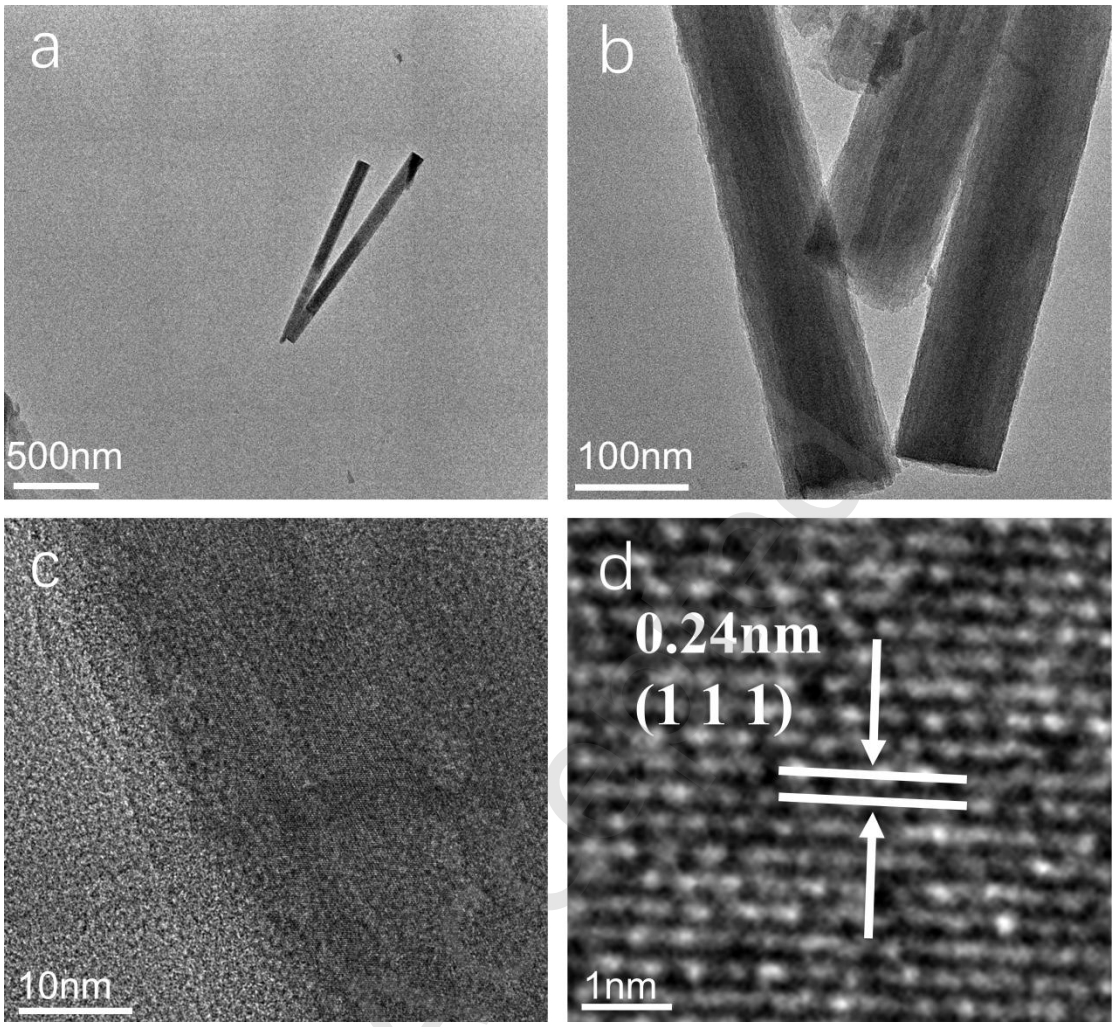

Fig. S3 (a, b) TEM and (c, d) HRTEM images of NiCo-LDH.

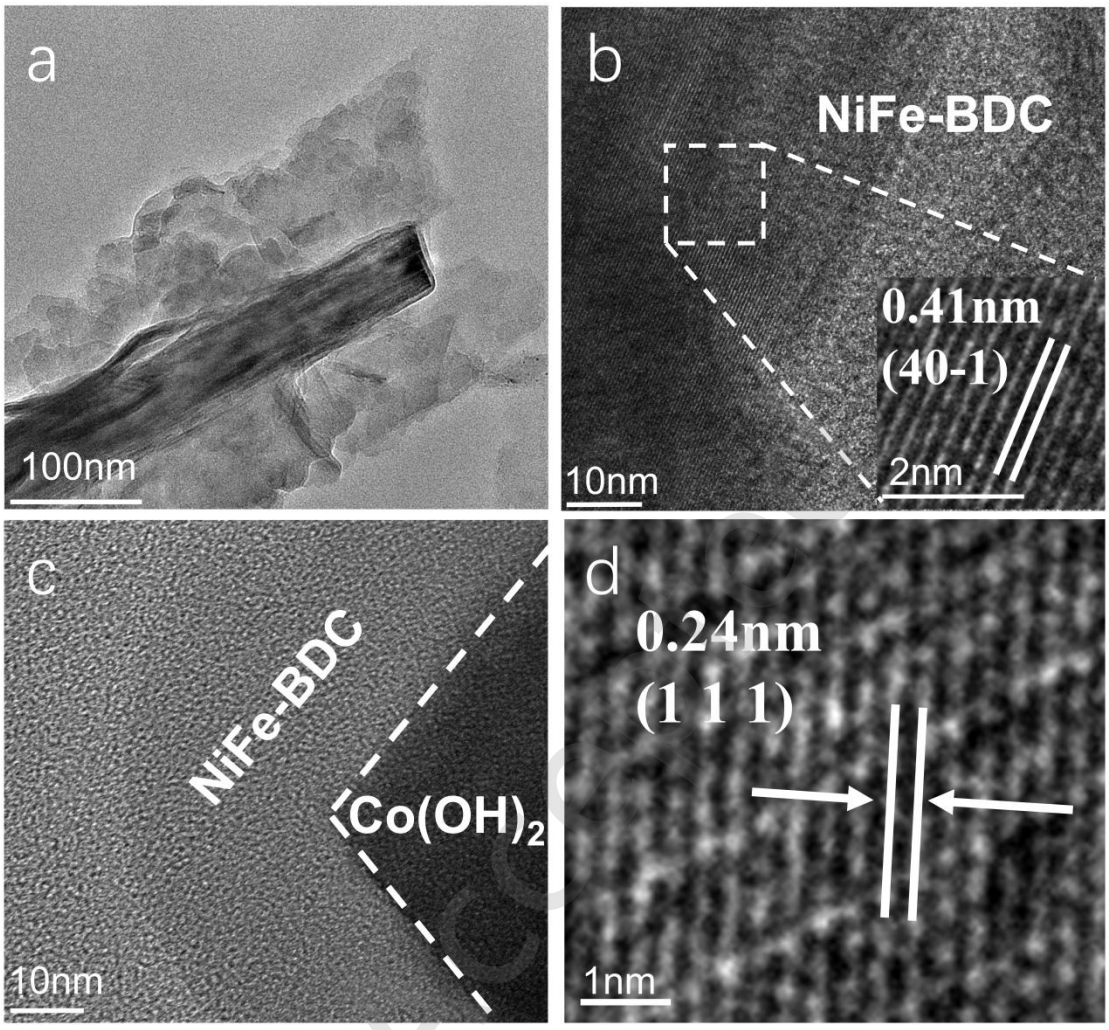

Fig. S4 (a) TEM and (b-d) HRTEM images of NiCo-LDH/NiFe-BDC.

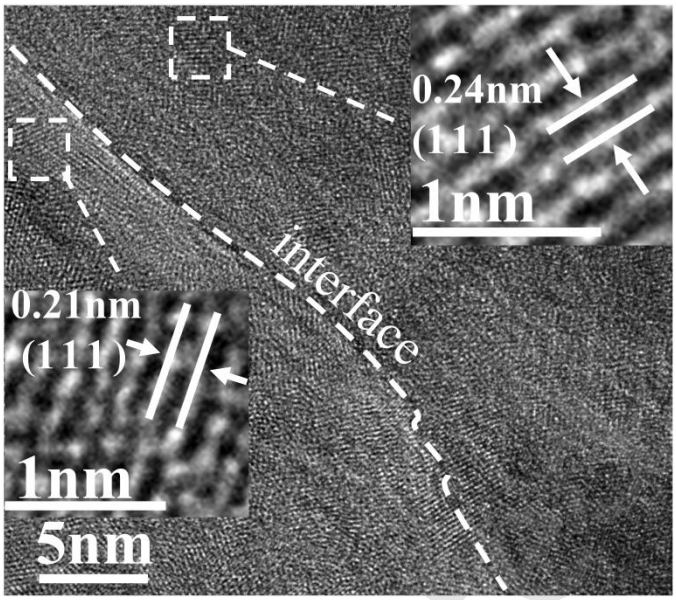

Fig. S5 HRTEM image of reconstructed NiCo-LDH/NiFe-BDC.

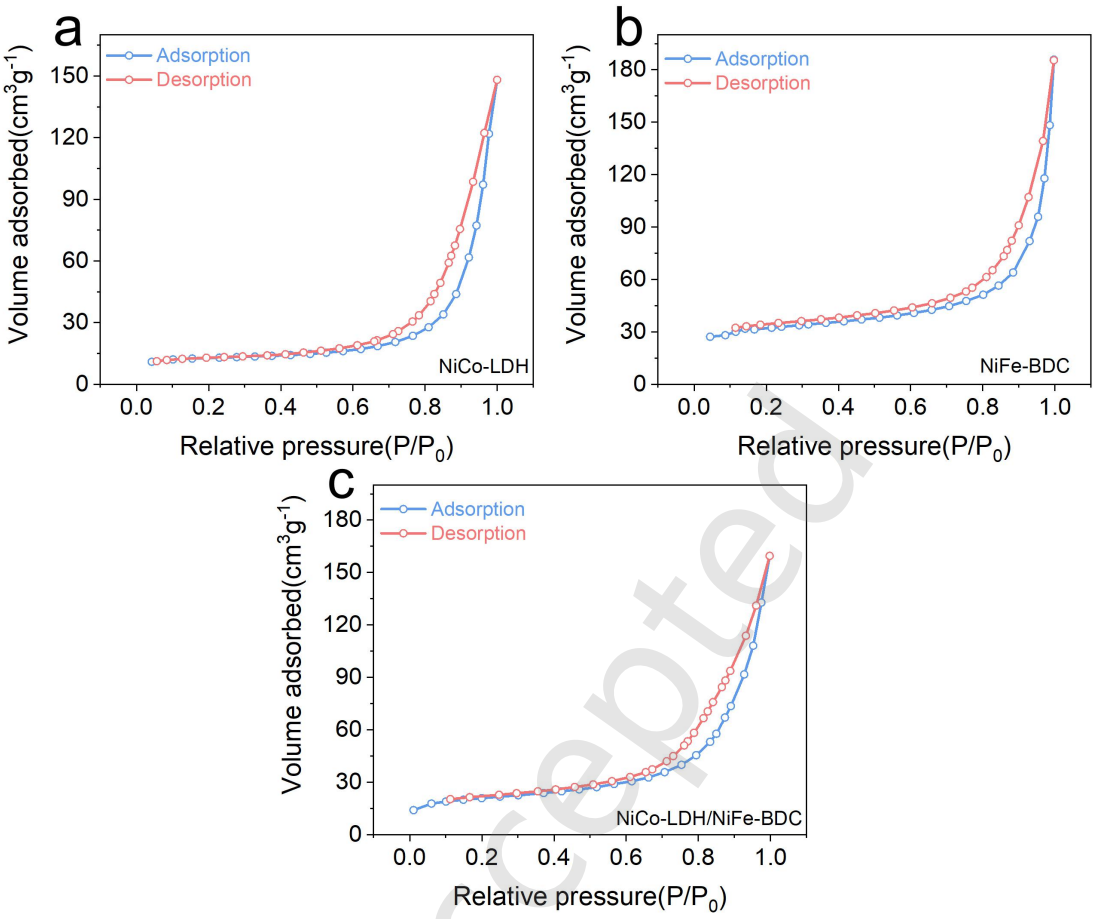

Fig. S6 N_2 adsorption-desorption isotherms of (a) NiCo-LDH, (b) NiFe-BDC, and (c) NiCo-LDH/ NiFe-BDC.

Table S1. Porosity properties of NiCo-LDH, NiFe-BDC, and NiCo-LDH/NiFe-BDC catalysts.

Catalyst	BET Suface Area (m^2/g)	Pore Volume (cm^3/g)	Average Pore size (nm)
NiCo-LDH	62	0.1	7.2
NiFe-BDC	104	0.08	17.6
NiCo-LDH/NiFe-BDC	89	0.11	15.5

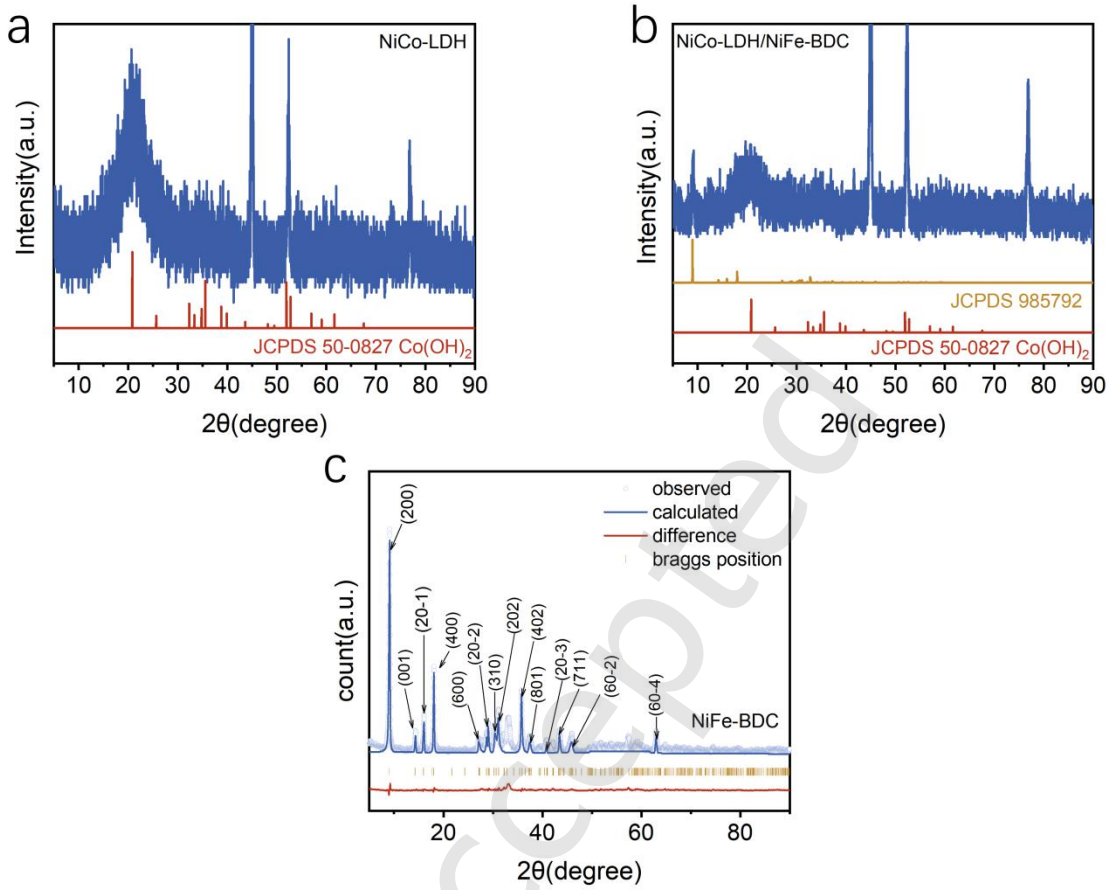

Fig.S7 XRD patterns of (a) NiCo-LDH and (b) NiCo-LDH/NiFe-BDC and refined spectrum of NiFe-BDC.

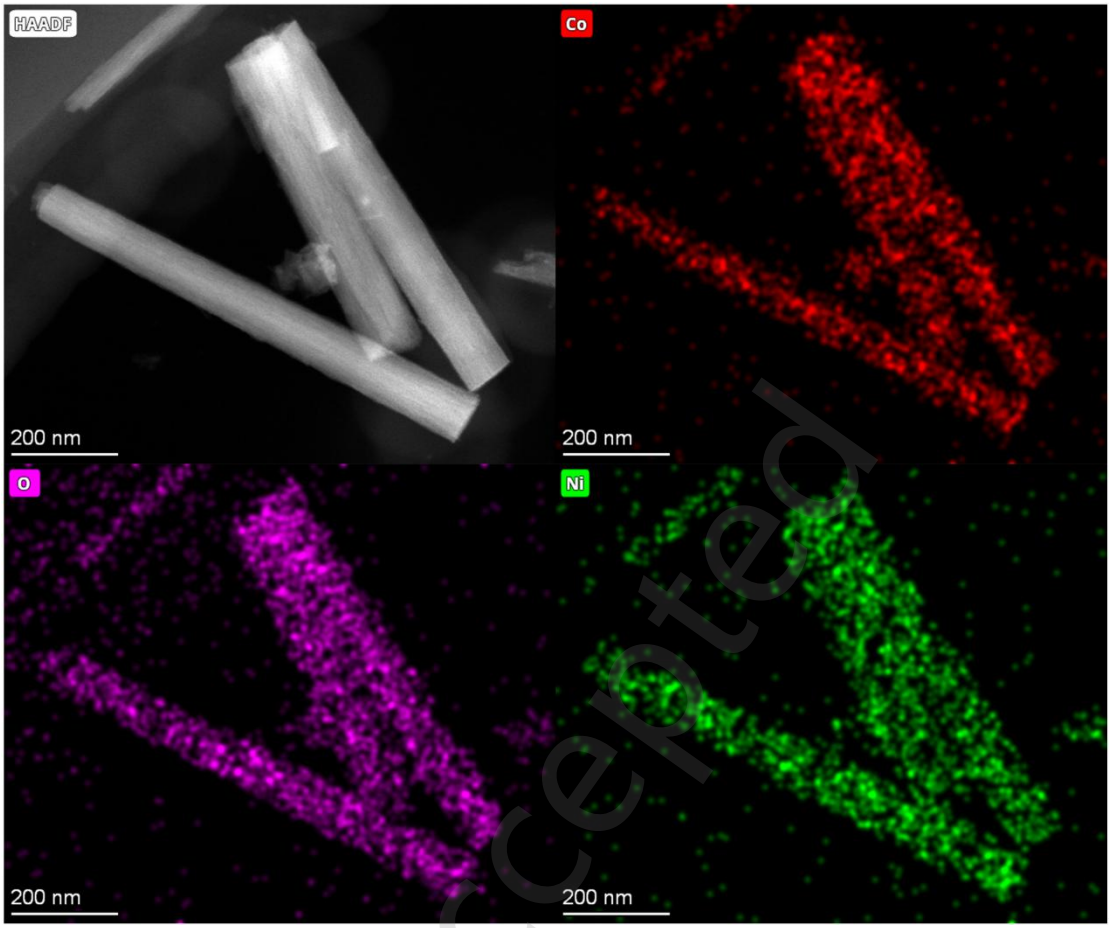

Fig. S8 EDS elemental mapping of NiCo-LDH.

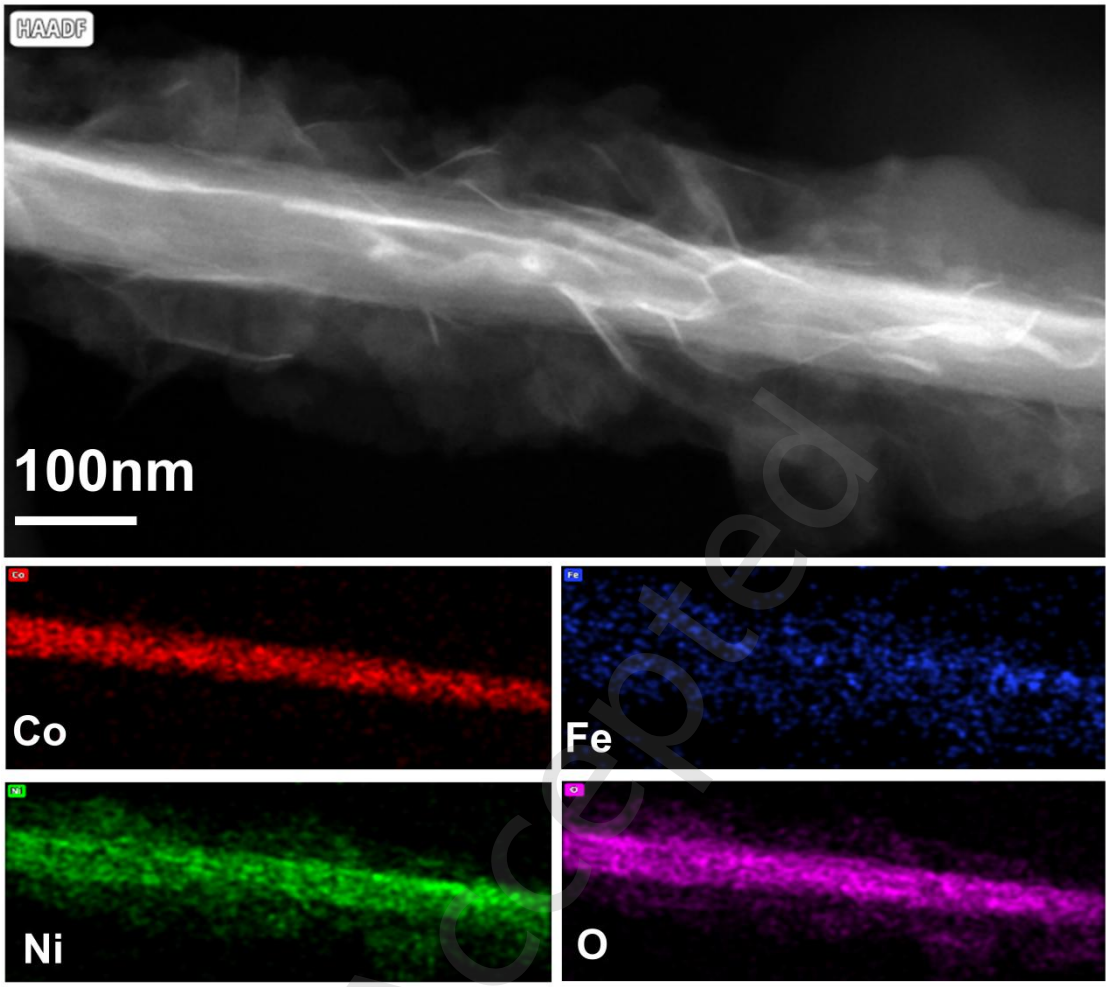

Fig. S9 EDS elemental mapping of NiCo-LDH/NiFe-BDC.

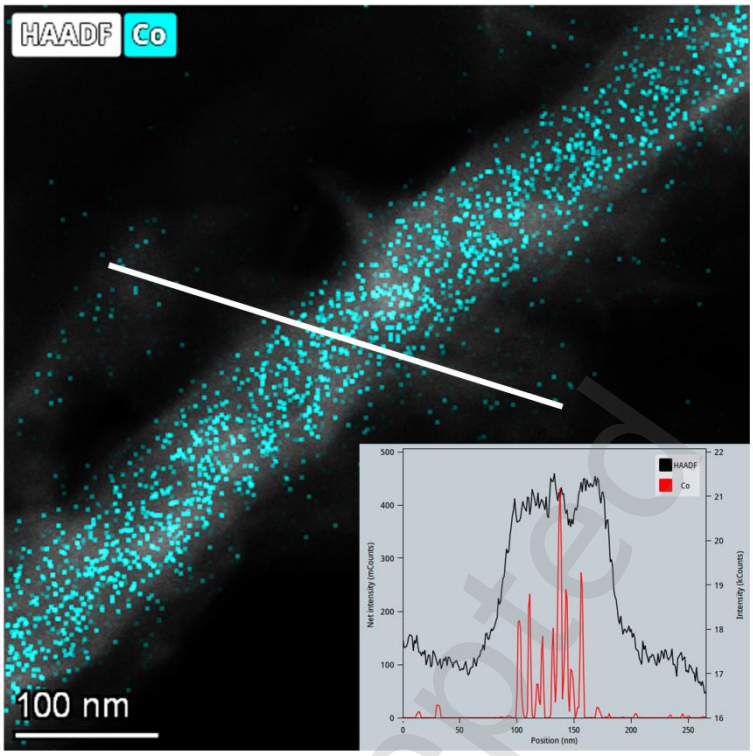

Fig. S10 Line-scan EDS elemental distribution of Co element along a reconstructed NiCo-LDH/NiFe-BDC nanorod.

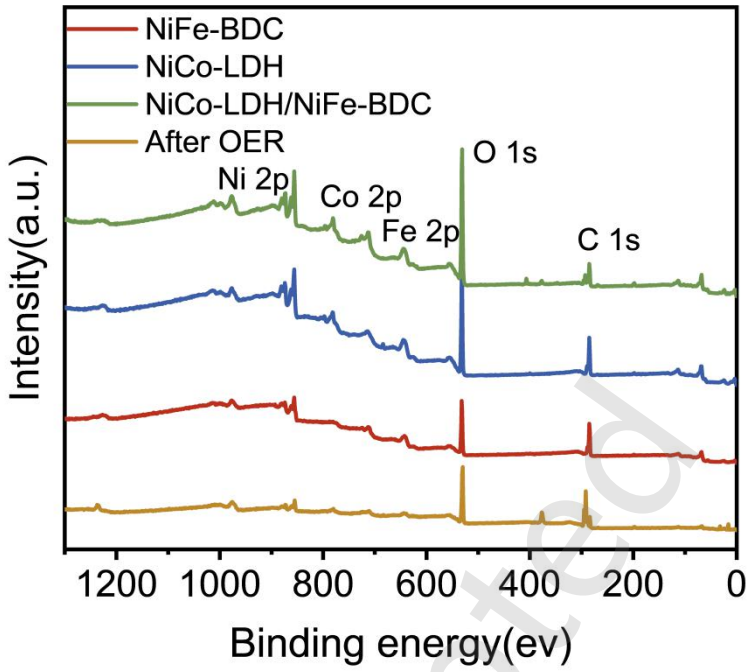

Fig. S11 XPS survey spectra of NiFe-BDC, NiCo-LDH, NiCo-LDH/NiFe-BDC and reconstructed NiCo-LDH/NiFe-BDC.

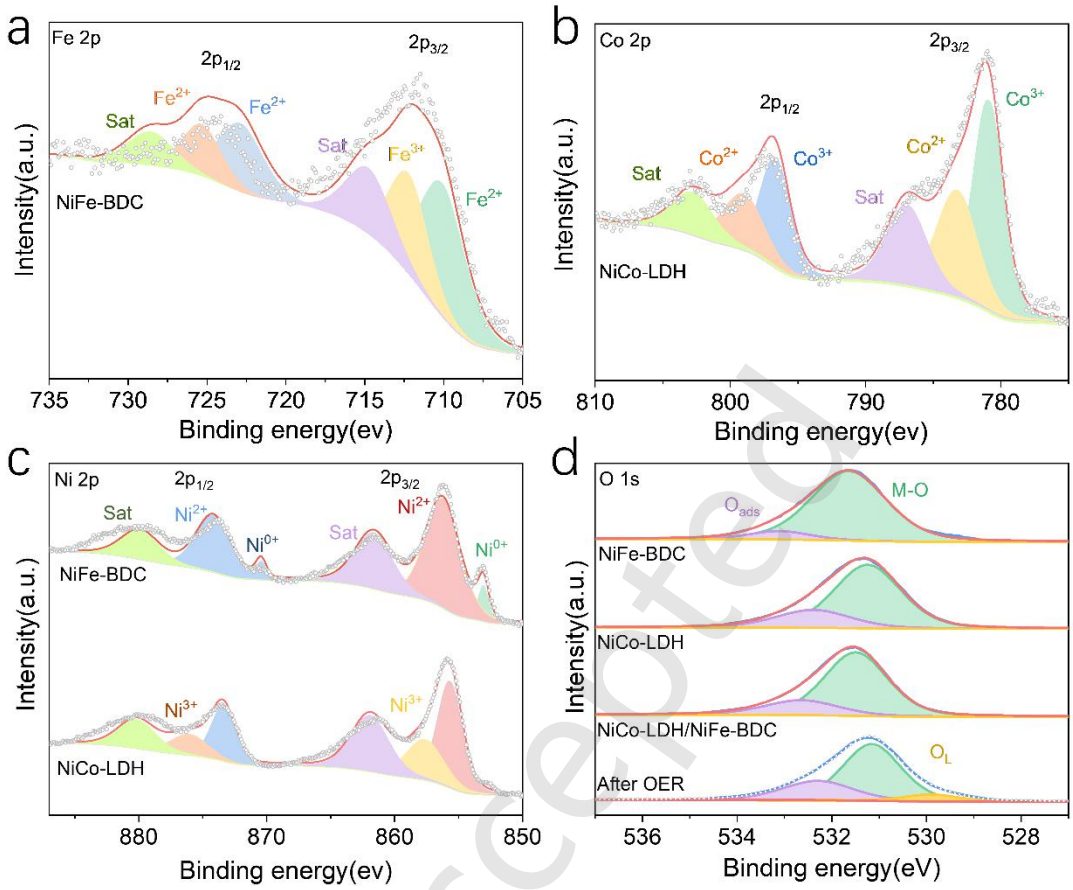

Fig. S12 High-resolution XPS (a) Fe 2p spectrum of NiFe-BDC, (b) Co 2p spectrum of NiCo-LDH, (c) Ni 2p spectra of NiFe-BDC and NiCo-LDH, and (d) O 1s spectra of NiFe-BDC, NiCo-LDH, NiCo-LDH/NiFe-BDC and reconstructed NiCo-LDH/NiFe-BDC.

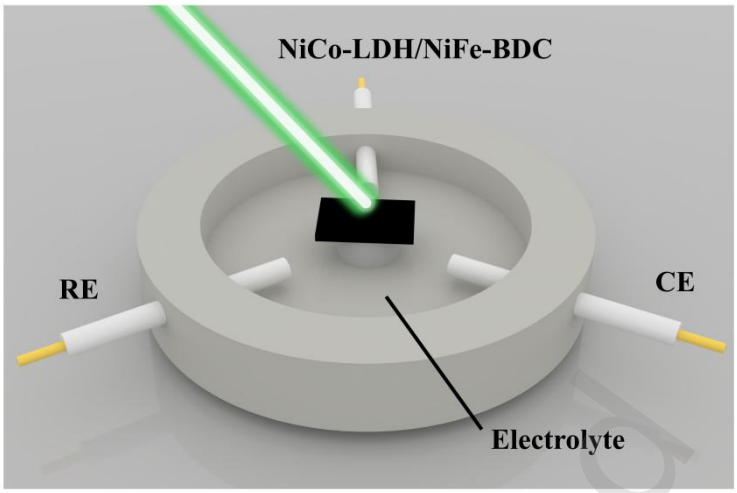

Fig. S13 Schematic diagram of *in-situ* Raman measurement.

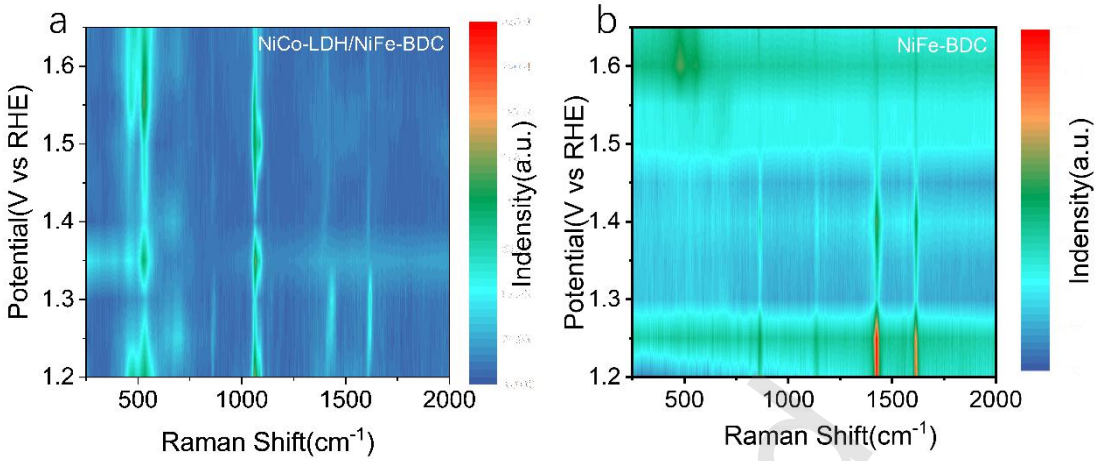

Fig. S14 Corresponding contour plots of *in-situ* Raman spectra of (a) NiCo-LDH/NiFe-BDC and (b) NiFe-BDC.

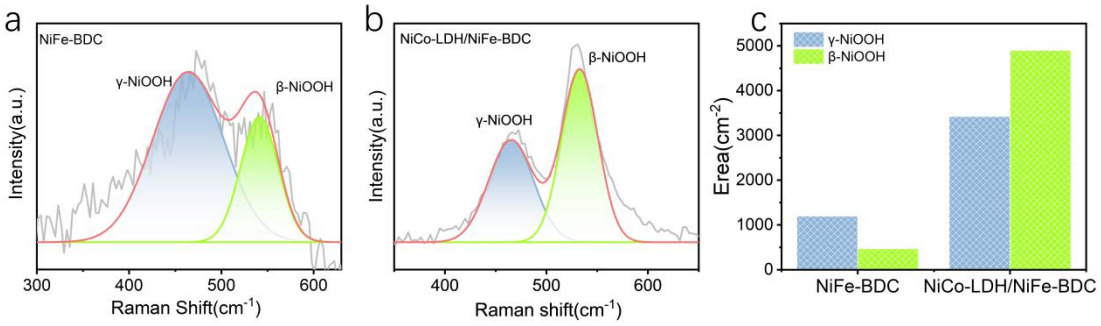

Fig. S15 The peak fitting result of E_g (476 cm^{-1}) and A_{1g} (554 cm^{-1}) modes for (a) NiFe-BDC and (b) NiCo-LDH/NiFe-BDC. (c) $\boldsymbol{I_{E_g}}$ / $\boldsymbol{I_{A_{1g}}}$ of NiFe-BDC and (b) NiCo-LDH/NiFe-BDC obtained from Raman spectra.

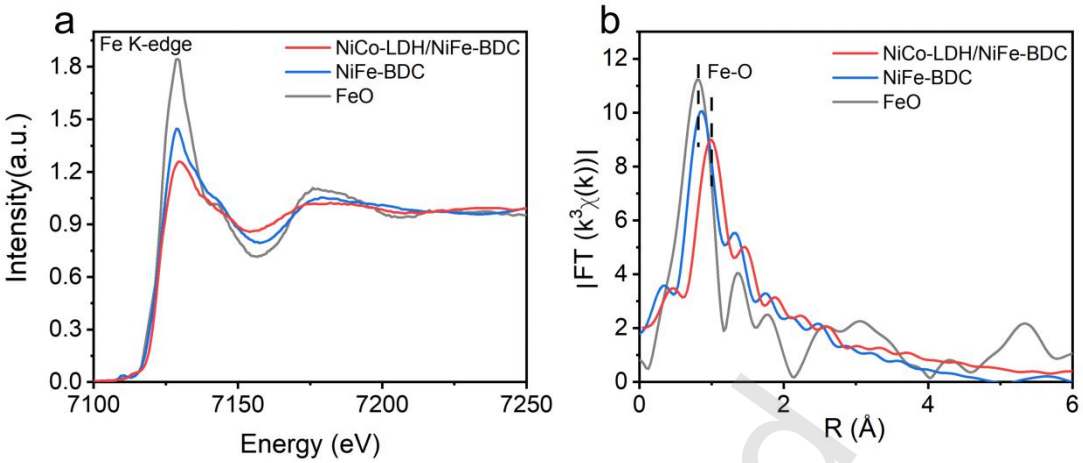

Fig. S16 (a) Fe K-edge XANES spectra, (b) Fourier transform of the extended XAFS (FT-EXAFS) spectra of NiFe-BDC, NiCo-LDH/NiFe-BDC, and FeO.

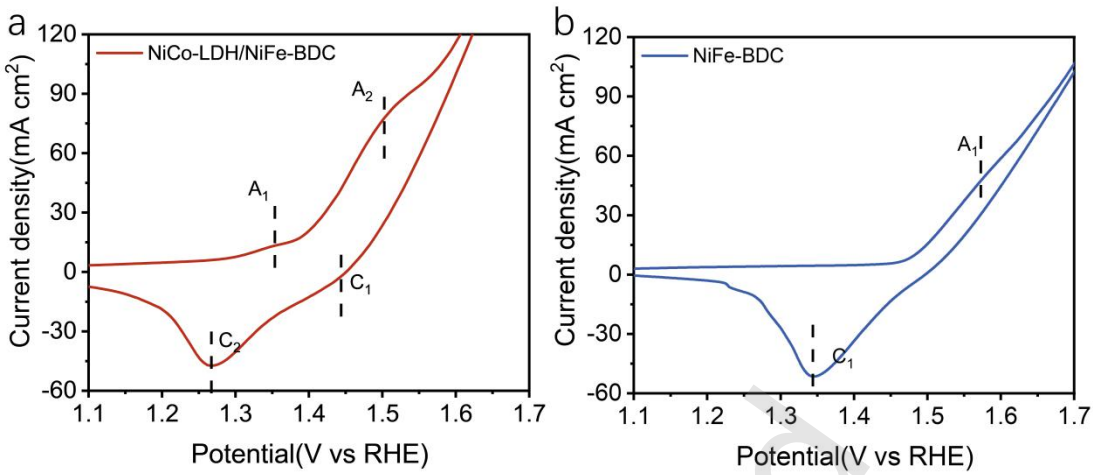

Fig. S17 CV curves of (a) NiCo-LDH/NiFe -BDC and (b) NiFe -BDC.

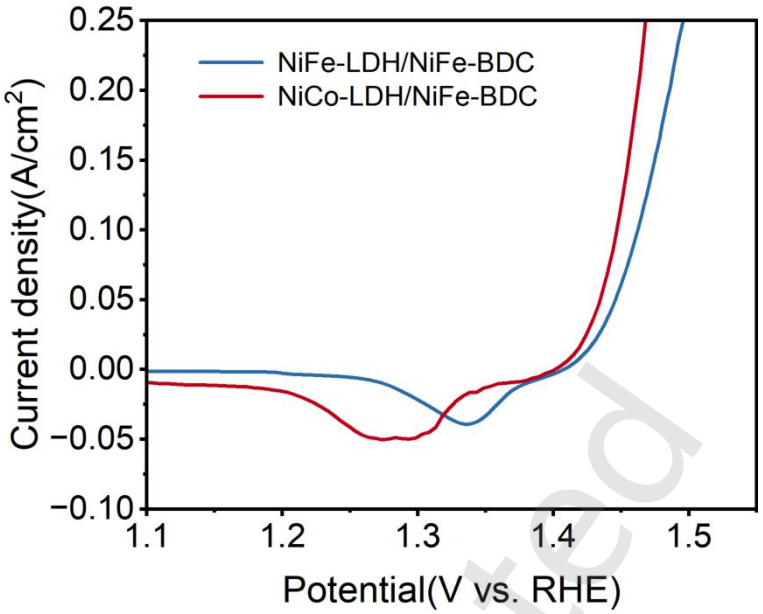

Fig. S18 LSV curves of NiFe-LDH/NiFe-BDC and NiCo-LDH/NiFe-BDC with for OER.

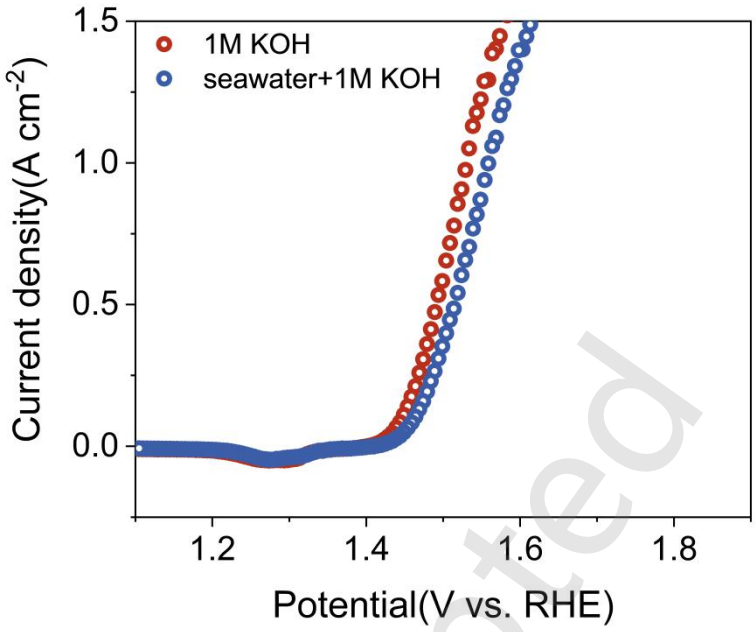

Fig. S19 Polarization curves of NiCo-LDH/NiFe-BDC in alkaline water and seawater.

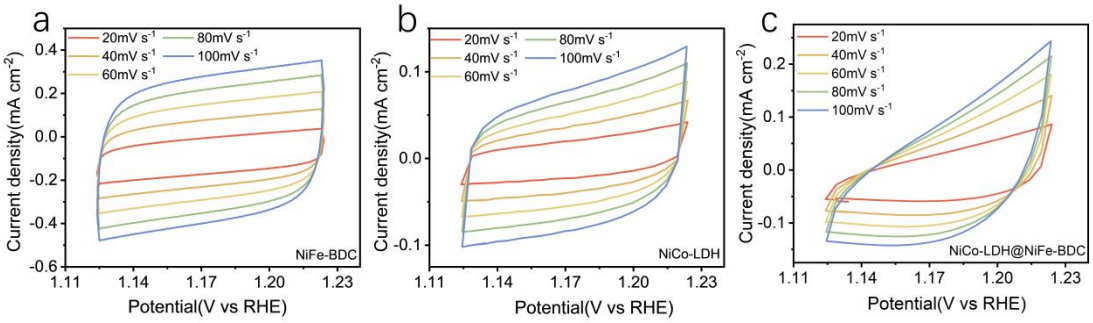

Fig. S20 CV curves at various scan rates of 20, 40, 60, 80, and 100 mV s^{-1} for (a) NiFe-BDC, (b) NiCo-LDH and (c) NiCo-LDH/NiFe-BDC.

Tabel S2. EIS fitting results of NiCo-LDH/NiFe-BDC, NiCo-LDH and NiFe-BDC obtained from Fig 3e.

Catalyst	Rs (Ω)	Rct (Ω)	CPE-T	CPE-P
NiCo-LDH/NiFe-BDC	1.1	1.2	0.8	0.5
NiCo-LDH	1	＞6	1.9	0.7
NiFe-BDC	1.1	1.8	1.2	0.7

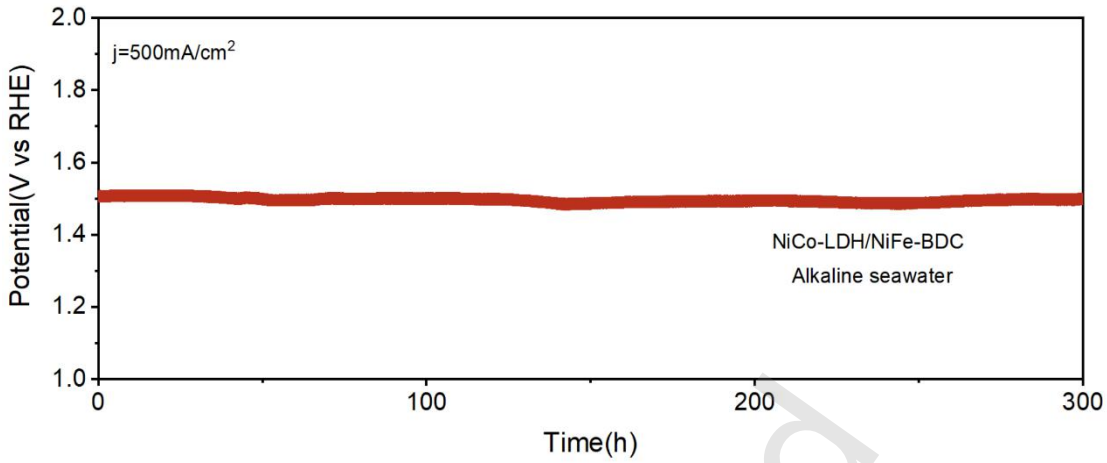

Fig. S21 Stability test at 500 mA cm^{-2} in alkaline seawater.

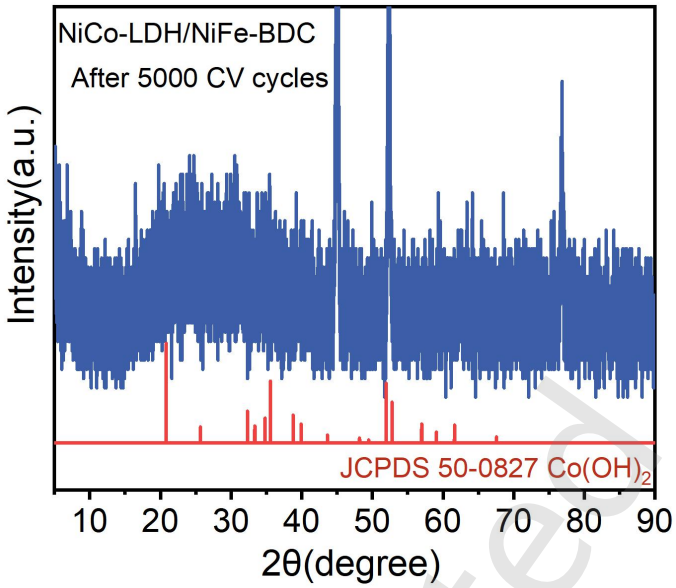

Fig. S22 XRD patterns of NiCo-LDH/NiFe-BDC after the long-term stability test.

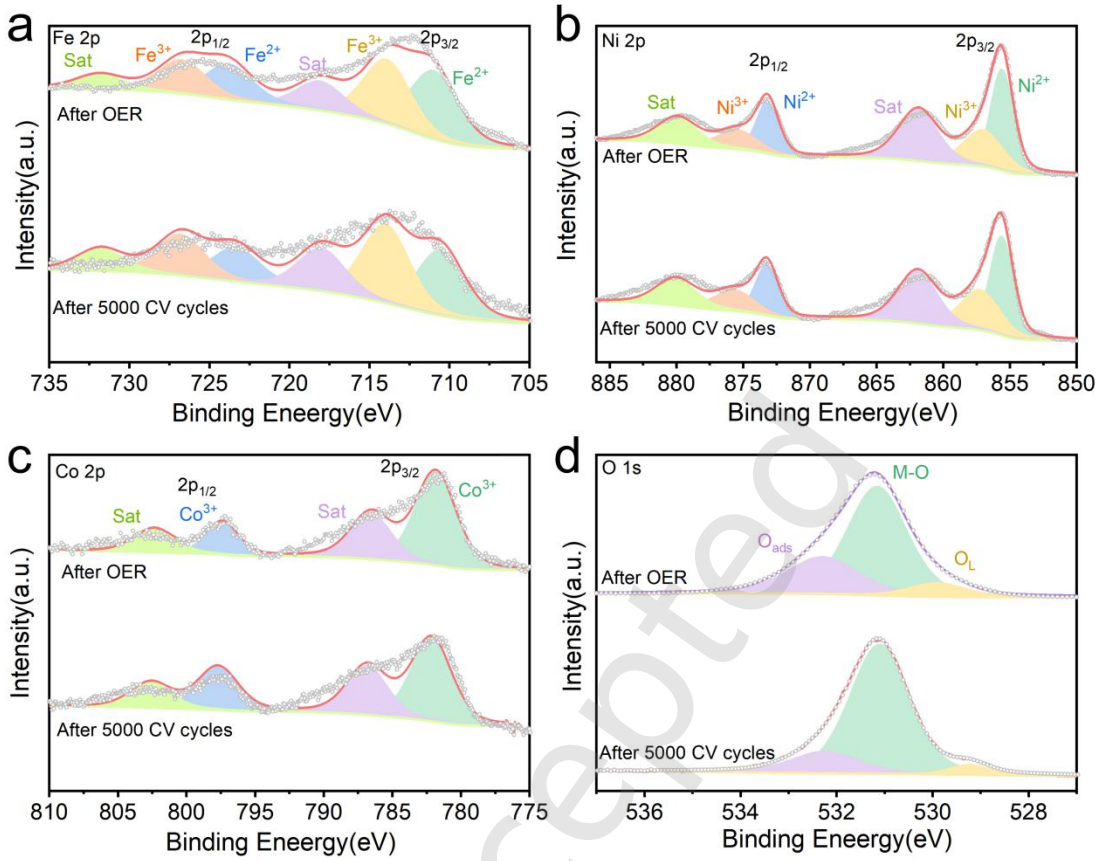

Fig. S23 High-resolution XPS spectra of (a) Fe 2p, (b) Ni 2p, (c)Co 2p and (d) O 1s for NiCo-LDH/NiFe-BDC after 5000 CV cycles and long-term stability test.

Table S3 Comparison of the OER performance with reported transition-metal-based electrocatalysts at 10 mA cm^{-2} in 1 M KOH.

Catalysts	η_{10} (mV)	Tafel (mV dec^{-1})	References
NiCo-LDH/NiFe-BDC	180	19	This work
NiFe-BDC	210	21.6	[15]
$(Ni_2Co_1)_{0.925}Fe_{0.075}$-MOF	257	41.3	[16]
FeCu-BTC/WO_3-WC	249	22.8	[17]
NiFeCo-NDA	215	64.1	[18]
W_2N/WC	320	94.5	[19]
Co_6W_6C@N	286	53.96	[20]
Ni_2W_4C-W_3C	270	52	[21]
e/FeNiOOH-NC	220	52	[22]
POM@ZnCoS/NF	224	67.7	[23]
CuFe composi	218	62.07	[24]
H-CoSx@NiFe	250	49	[25]
NiS_2/MoS_2	270	119	[26]
Mo_2NiB_2	280	57	[27]
IW-Co_3O_4-RuO_2-HS	250	55.4	[28]
RuCoOx	275	54	[29]
S/N-CMF@$Fe_xCo_yNi_{1-x-y}$MOF	296	53.5	[30]
$Ni_{65}Fe_{35}$(OOH)	316	38	[31]
NiMn-MOFs	280	86	[32]
CoNi-MOFNA	215	51.6	[33]
NiFe-MOF-BF_4^--0.3 NS_S	237	41	[34]
Co_1Ni_3 sq-zbr-MOF	230	37.7	[35]
MIL-53(Fe)-2OH	215	45.5	[36]

DD-Ni-NDA	260	50	[37]

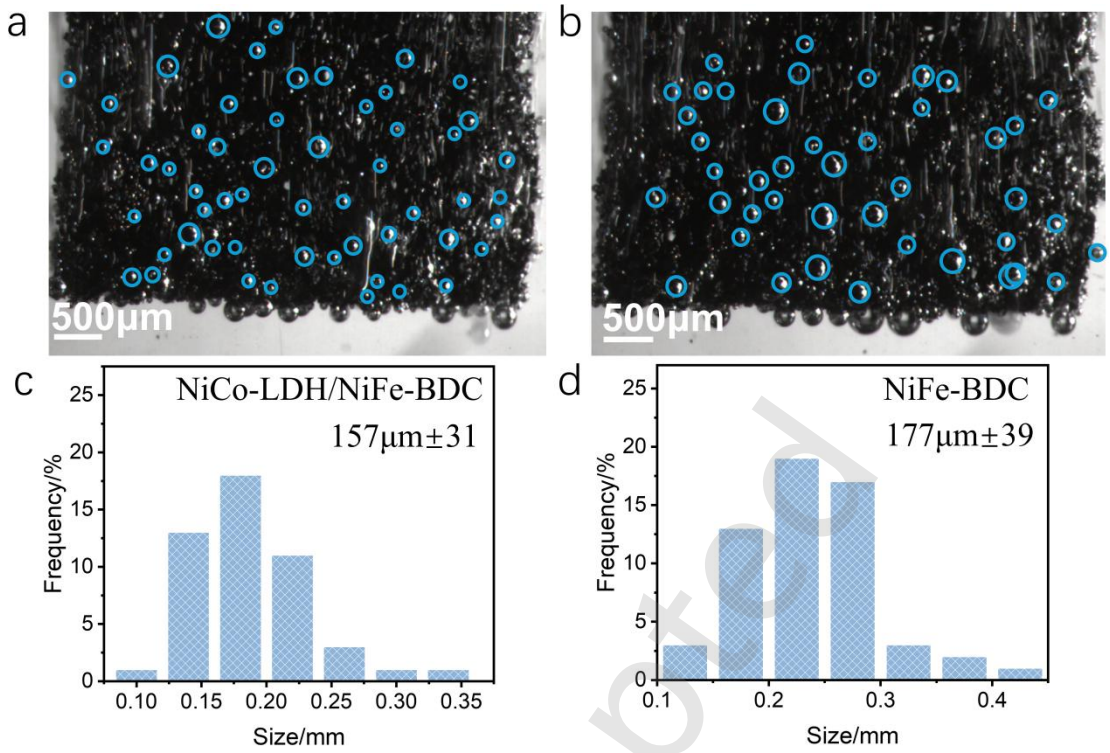

Fig. S24 Digital photos of (a) NiCo-LDH/NiFe-BDC and (b) NiFe-BDC during OER. Size distribution of releasing bubbles on (c) NiCo-LDH/NiFe-BDC and (d) NiFe-BDC.

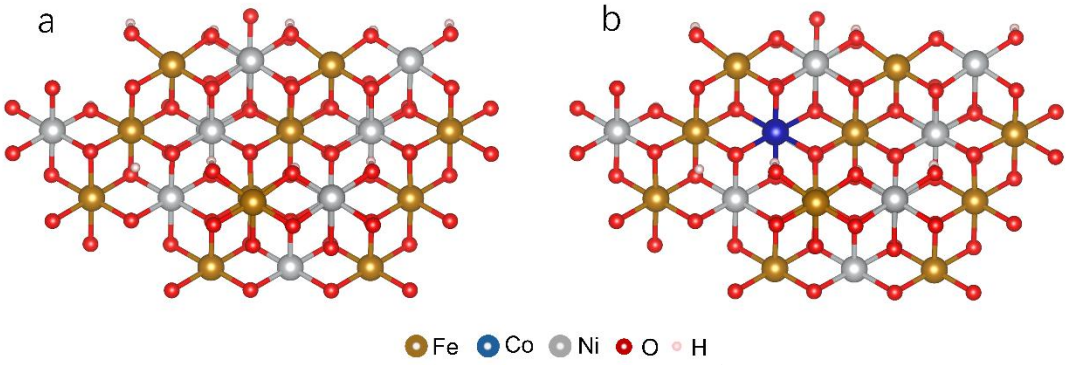

Fig. S25 Optimized structure models of (a) NiFeOOH and (b) Co-NiFeOOH

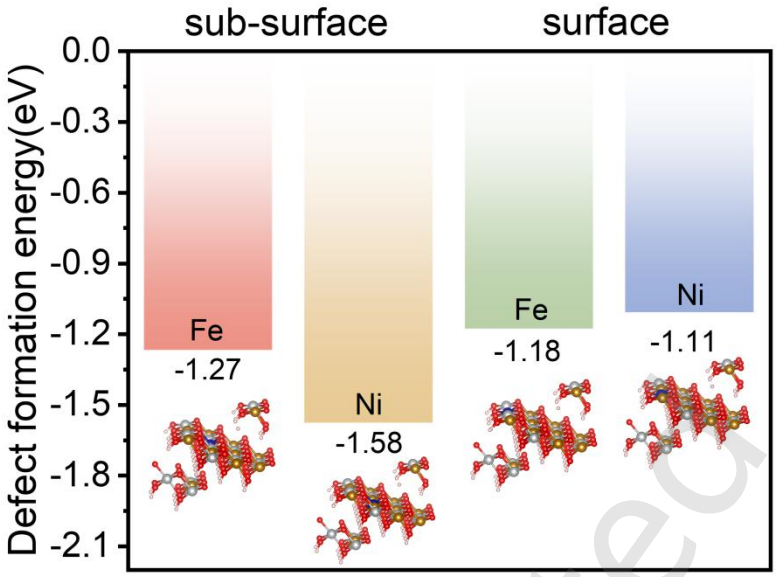

Fig. S26 Defect formation energy comparison for Co substituted NiFeOOH surface at different sites.

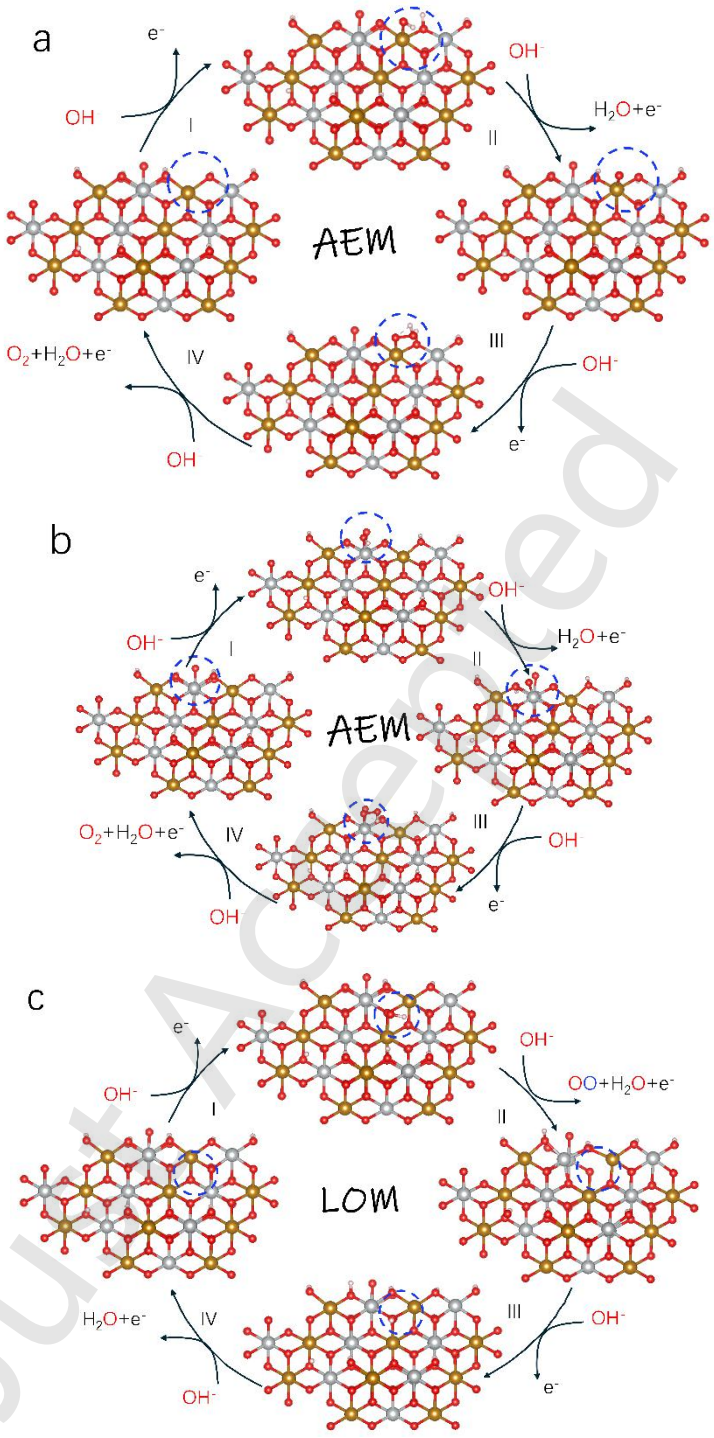

Fig. S27 AEM pathway on the NiFeOOH electrocatalyst: (a) Fe site, (b) Ni site. (c) LOM pathway on the NiFeOOH electrocatalyst.

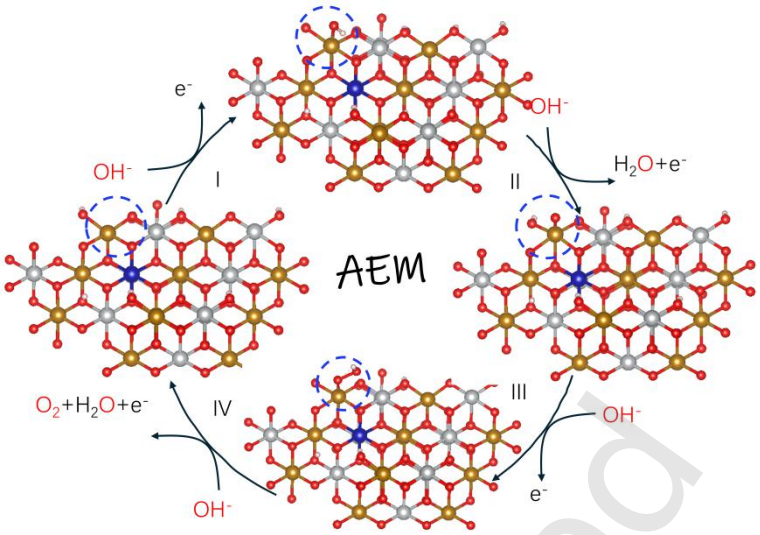

Fig. S28 AEM pathway on the Co-NiFeOOH electrocatalyst (Fe site).

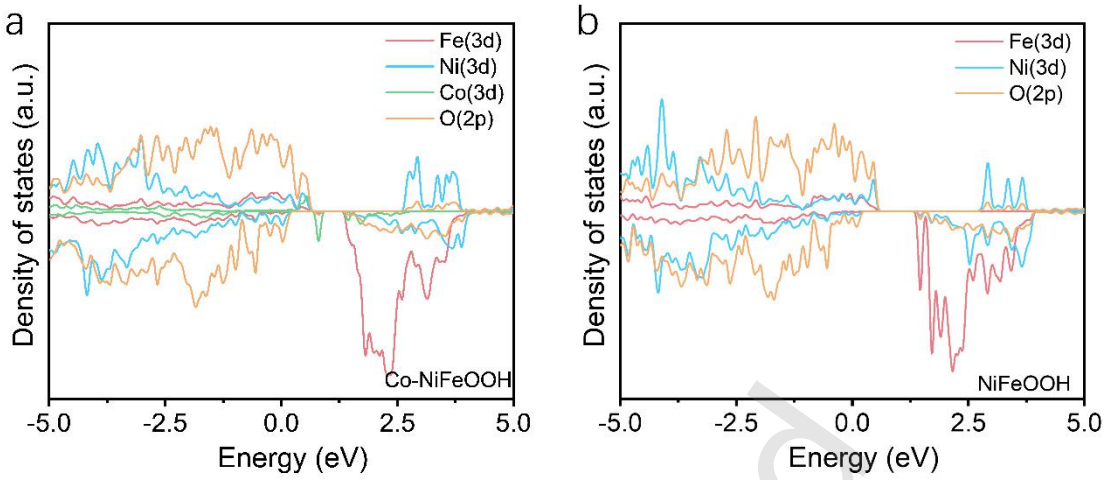

Fig. S29 PDOS of the surface (a) Fe 3d, Ni 3d, Co 3d, O 2p orbitals for Co-NiFeOOH and (b) Fe 3d, Ni 3d, O 2p orbitals for NiFeOOH.

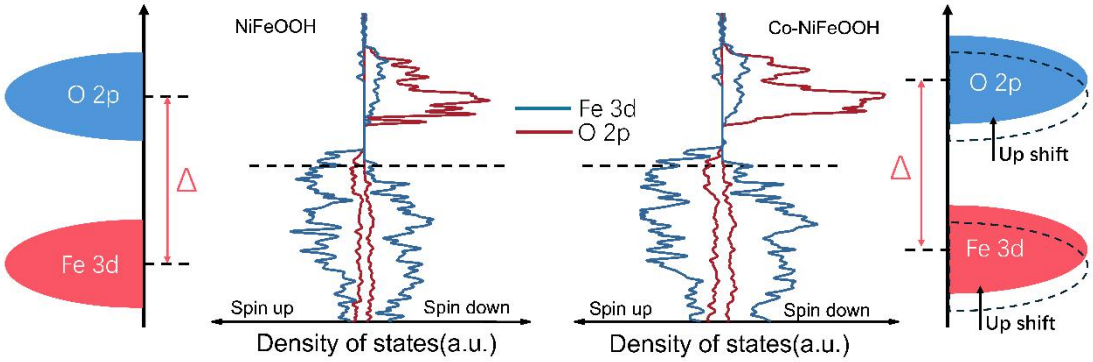

Fig. S30 The schematic band diagrams and density of states of NiFeOOH and Co-NiFeOOH.

References

[1] Kohn, W.; Sham, L. J. Self-Consistent Equations Including Exchange and Correlation Effects. *Physical Review* **1965**, *140*, A1133-A1138.

[2] Kresse, G.; Furthmüller, J. Efficient iterative schemes for ab initio total-energy calculations using a plane-wave basis set. *Physical Review B* **1996**, *54*, 11169-11186.

[3] Blöchl, P. E. Projector augmented-wave method. *Physical Review B* **1994**, *50*, 17953-17979.

[4] Perdew, J. P.;Burke, K.; Ernzerhof, M. Generalized Gradient Approximation Made Simple. *Phys. Rev. Lett.* **1996**, *77*, 3865-3868.

[5] Mei, Y.;Chen, J.;Wang, Q.;Guo, Y.;Liu, H.;Shi, W.;Lin, C.;Yuan, Y.;Wang, Y.;Xia, B. Y.; Yao, Y. MoZn-based high entropy alloy catalysts enabled dual activation and stabilization in alkaline oxygen evolution. *Science Advances* **2024**, *10*, eadq6758.

[6] Grimme, S.;Antony, J.;Ehrlich, S.; Krieg, H. A consistent and accurate ab initio parametrization of density functional dispersion correction (DFT-D) for the 94 elements H-Pu. *The Journal of Chemical Physics* **2010**, *132*, 154104.

[7] Monkhorst, H. J.; Pack, J. D. Special points for Brillouin-zone integrations. *Physical Review B* **1976**, *13*, 5188-5192.

[8] Sanville, E.;Kenny, S. D.;Smith, R.; Henkelman, G. Improved grid-based algorithm for Bader charge allocation. *J. Comput. Chem.* **2007**, *28*, 899-908.

[9] Hjorth Larsen, A.;Jørgen Mortensen, J.;Blomqvist, J.;Castelli, I. E.;Christensen, R.;Dułak, M.;Friis, J.;Groves, M. N.;Hammer, B.;Hargus, C.;Hermes, E. D.;Jennings, P. C.;Bjerre Jensen, P.;Kermode, J.;Kitchin, J. R.;Leonhard Kolsbjerg, E.;Kubal, J.;Kaasbjerg, K.;Lysgaard, S.;Bergmann Maronsson, J.;Maxson, T.;Olsen, T.;Pastewka, L.;Peterson, A.;Rostgaard, C.;Schiøtz, J.;Schütt, O.;Strange, M.;Thygesen, K. S.;Vegge, T.;Vilhelmsen, L.;Walter, M.;Zeng, Z.; Jacobsen, K. W. The atomic simulation environment—a Python library for working with atoms. *J. Phys.: Condens. Matter* **2017**, *29*, 273002.

[10] Nørskov, J. K.;Rossmeisl, J.;Logadottir, A.;Lindqvist, L.;Kitchin, J. R.;Bligaard, T.; Jónsson, H. Origin of the Overpotential for Oxygen Reduction at a Fuel-Cell Cathode. *The Journal of Physical Chemistry B* **2004**, *108*, 17886-17892.

[11] Prabhu, P.;Do, V.-H.;Yoshida, T.;Zhou, Y.;Ariga-Miwa, H.;Kaneko, T.;Uruga, T.;Iwasawa, Y.; Lee, J.-M. Subnanometric Osmium Clusters Confined on Palladium Metallenes for Enhanced Hydrogen Evolution and Oxygen Reduction Catalysis. *ACS Nano* **2024**, *18*, 9942-9957.

[12] Hansen, H. A.;Man, I. C.;Studt, F.;Abild-Pedersen, F.;Bligaard, T.; Rossmeisl, J. Electrochemical chlorine evolution at rutile oxide (110) surfaces. *Physical Chemistry Chemical Physics* **2010**, *12*, 283-290.

[13] Yu, Y.;Zhou, W.;Zhou, X.;Yuan, J.;Zhang, X.;Wang, L.;Li, J.;Meng, X.;Sun, F.;Gao, J.; Zhao, G. The Corrosive Cl–-Induced Rapid Surface Reconstruction of Amorphous NiFeCoP Enables Efficient Seawater Splitting. *ACS Catalysis* **2024**, *14*, 18322-18332.

[14] Liu, Y.;Li, C.;Tan, C.;Pei, Z.;Yang, T.;Zhang, S.;Huang, Q.;Wang, Y.;Zhou, Z.;Liao, X.;Dong, J.;Tan, H.;Yan, W.;Yin, H.;Liu, Z.-Q.;Huang, J.; Zhao, S. Electrosynthesis of chlorine from seawater-like solution through single-atom catalysts. *Nature Communications* **2023**, *14*, 2475.

[15] Na, G.;Wu, Y.;Mei, Z.;Chen, M.;Dequan, L.;Sun, H.;Chen, Y.;Zhou, T.;Zhao, J.;Zhang, Y.;Zhang, J.;Liu, F.;Cui, H.; Liu, Q. Construction of trimetallic metal-organic framework nanoarrays for efficient and stable oxygen evolution reaction. *Int. J. Hydrogen Energy* **2024**, *86*, 1278-1284.

[16] Qian, Q.;Li, Y.;Liu, Y.;Yu, L.; Zhang, G. Ambient Fast Synthesis and Active Sites Deciphering of Hierarchical Foam-Like Trimetal–Organic Framework Nanostructures as a Platform for Highly Efficient Oxygen Evolution Electrocatalysis. *Adv. Mater.* **2019**, *31*, 1901139.

[17] Paudel, D. R.;Pan, U. N.;Ghising, R. B.;Kandel, M. R.;Prabhakaran, S.;Kim, D. H.;Kim, N. H.; Lee, J. H. Multi-interfacial dendritic engineering facilitating congruous intrinsic activity of oxide-carbide/MOF nanostructured multimodal

electrocatalyst for hydrogen and oxygen electrocatalysis. *Applied Catalysis B: Environmental* **2023**, *331*, 122711.

[18] Yue, K.;Liu, J.;Zhu, Y.;Xia, C.;Wang, P.;Zhang, J.;Kong, Y.;Wang, X.;Yan, Y.; Xia, B. Y. In situ ion-exchange preparation and topological transformation of trimetal–organic frameworks for efficient electrocatalytic water oxidation. *Energy & Environmental Science* **2021**, *14*, 6546-6553.

[19] Diao, J.;Qiu, Y.;Liu, S.;Wang, W.;Chen, K.;Li, H.;Yuan, W.;Qu, Y.; Guo, X. Interfacial Engineering of W2N/WC Heterostructures Derived from Solid-State Synthesis: A Highly Efficient Trifunctional Electrocatalyst for ORR, OER, and HER. *Adv. Mater.* **2020**, *32*, 1905679.

[20] Chen, J.;Ren, B.;Cui, H.; Wang, C. Constructing Pure Phase Tungsten-Based Bimetallic Carbide Nanosheet as an Efficient Bifunctional Electrocatalyst for Overall Water Splitting. *Small* **2020**, *16*, 1907556.

[21] Zhang, S.;Gao, G.;Zhu, H.;Cai, L.;Jiang, X.;Lu, S.;Duan, F.;Dong, W.;Chai, Y.; Du, M. In situ interfacial engineering of nickel tungsten carbide Janus structures for highly efficient overall water splitting. *Science Bulletin* **2020**, *65*, 640-650.

[22] Ibraheem, S.;Li, X.;Shah, S. S. A.;Najam, T.;Yasin, G.;Iqbal, R.;Hussain, S.;Ding, W.; Shahzad, F. Tellurium Triggered Formation of Te/Fe-NiOOH Nanocubes as an Efficient Bifunctional Electrocatalyst for Overall Water Splitting. *ACS Applied Materials & Interfaces* **2021**, *13*, 10972-10978.

[23] Gautam, J.;Liu, Y.;Gu, J.;Ma, Z.;Zha, J.;Dahal, B.;Zhang, L.-N.;Chishti, A. N.;Ni, L.;Diao, G.; Wei, Y. Fabrication of Polyoxometalate Anchored Zinc Cobalt Sulfide Nanowires as a Remarkable Bifunctional Electrocatalyst for Overall Water Splitting. *Adv. Funct. Mater.* **2021**, *31*, 2106147.

[24] Inamdar, A. I.;Chavan, H. S.;Hou, B.;Lee, C. H.;Lee, S. U.;Cha, S.;Kim, H.; Im, H. A Robust Nonprecious CuFe Composite as a Highly Efficient Bifunctional Catalyst for Overall Electrochemical Water Splitting. *Small* **2020**, *16*, 1905884.

[25] Lee, Y. J.; Park, S.-K. Metal–Organic Framework-Derived Hollow CoSx

Nanoarray Coupled with NiFe Layered Double Hydroxides as Efficient Bifunctional Electrocatalyst for Overall Water Splitting. *Small* **2022**, *18*, 2200586.

[26] Zeng, J.;Zhang, L.;Zhou, Q.;Liao, L.;Qi, Y.;Zhou, H.;Li, D.;Cai, F.;Wang, H.;Tang, D.; Yu, F. Boosting Alkaline Hydrogen and Oxygen Evolution Kinetic Process of Tungsten Disulfide-Based Heterostructures by Multi-Site Engineering. *Small* **2022**, *18*, 2104624.

[27] Qian, Y.;Yu, J.;Zhang, Y.;Zhang, F.;Kang, Y.;Su, C.;Shi, H.;Kang, D. J.; Pang, H. Interfacial Microenvironment Modulation Enhancing Catalytic Kinetics of Binary Metal Sulfides Heterostructures for Advanced Water Splitting Electrocatalysts. *Small Methods* **2022**, *6*, 2101186.

[28] Gao, Y.;Zheng, D.;Li, Q.;Xiao, W.;Ma, T.;Fu, Y.;Wu, Z.; Wang, L. 3D Co3O4-RuO2 Hollow Spheres with Abundant Interfaces as Advanced Trifunctional Electrocatalyst for Water-Splitting and Flexible Zn–Air Battery. *Adv. Funct. Mater.* **2022**, *32*, 2203206.

[29] Zhou, C.;Zhao, S.;Meng, H.;Han, Y.;Jiang, Q.;Wang, B.;Shi, X.;Zhang, W.;Zhang, L.; Zhang, R. RuCoOx Nanofoam as a High-Performance Trifunctional Electrocatalyst for Rechargeable Zinc–Air Batteries and Water Splitting. *Nano Lett.* **2021**, *21*, 9633-9641.

[30] Zhao, Y.;Lu, X. F.;Wu, Z.-P.;Pei, Z.;Luan, D.; Lou, X. W. Supporting Trimetallic Metal-Organic Frameworks on S/N-Doped Carbon Macroporous Fibers for Highly Efficient Electrocatalytic Oxygen Evolution. *Adv. Mater.* **2023**, *35*, 2207888.

[31] Görlin, M.;Halldin Stenlid, J.;Koroidov, S.;Wang, H.-Y.;Börner, M.;Shipilin, M.;Kalinko, A.;Murzin, V.;Safonova, O. V.;Nachtegaal, M.;Uheida, A.;Dutta, J.;Bauer, M.;Nilsson, A.; Diaz-Morales, O. Key activity descriptors of nickel-iron oxygen evolution electrocatalysts in the presence of alkali metal cations. *Nature Communications* **2020**, *11*, 6181.

[32] Cheng, W.;Lu, X. F.;Luan, D.; Lou, X. W. NiMn-Based Bimetal–Organic Framework Nanosheets Supported on Multi-Channel Carbon Fibers for

Efficient Oxygen Electrocatalysis. *Angew. Chem. Int. Ed.* **2020**, *59*, 18234-18239.

[33] Huang, L.;Gao, G.;Zhang, H.;Chen, J.;Fang, Y.; Dong, S. Self-dissociation-assembly of ultrathin metal-organic framework nanosheet arrays for efficient oxygen evolution. *Nano Energy* **2020**, *68*, 104296.

[34] Zhao, Z.-Y.;Sun, X.;Gu, H.;Niu, Z.;Braunstein, P.; Lang, J.-P. Engineering the Electronic Structures of Metal–Organic Framework Nanosheets via Synergistic Doping of Metal Ions and Counteranions for Efficient Water Oxidation. *ACS Applied Materials & Interfaces* **2022**, *14*, 15133-15140.

[35] Kandambeth, S.;Kale, V. S.;Fan, D.;Bau, J. A.;Bhatt, P. M.;Zhou, S.;Shkurenko, A.;Rueping, M.;Maurin, G.;Shekhah, O.; Eddaoudi, M. Unveiling Chemically Robust Bimetallic Squarate-Based Metal–Organic Frameworks for Electrocatalytic Oxygen Evolution Reaction. *Advanced Energy Materials* **2023**, *13*, 2202964.

[36] Zhang, C.;Qi, Q.;Mei, Y.;Hu, J.;Sun, M.;Zhang, Y.;Huang, B.;Zhang, L.; Yang, S. Rationally Reconstructed Metal–Organic Frameworks as Robust Oxygen Evolution Electrocatalysts. *Adv. Mater.* **2023**, *35*, 2208904.

[37] He, F.;Zheng, Q.;Yang, X.;Wang, L.;Zhao, Z.;Xu, Y.;Hu, L.;Kuang, Y.;Yang, B.;Li, Z.;Lei, L.;Qiu, M.;Lu, J.; Hou, Y. Spin-State Modulation on Metal–Organic Frameworks for Electrocatalytic Oxygen Evolution. *Adv. Mater.* **2023**, *35*, 2304022.